

1 **Estimating surface mass balance patterns from UAV measurements**  
2 **on the ablation area of the Morteratsch-Pers glacier complex**  
3 **(Switzerland)**  
4

5 Lander VAN TRICHT<sup>1,\*</sup>, Philippe HUYBRECHTS<sup>1</sup>, Jonas VAN BREEDAM<sup>1</sup>, Alexander  
6 VANHULLE<sup>1</sup>, Kristof VAN OOST<sup>2</sup>, Harry ZEKOLLARI<sup>3</sup>

7  
8 <sup>1</sup>Earth System Science & Departement Geografie, Vrije Universiteit Brussel, Brussels, Belgium

9 <sup>2</sup>Georges Lemaître Center for Earth & Climate Research, Earth and Life Institute, Université catholique de  
10 Louvain, Louvain-la-Neuve, Belgium

11 <sup>3</sup>Department of Geoscience and Remote Sensing, Delft University of Technology, Delft, Netherlands  
12

13 *\*Corresponding author: Lander Van Tricht ([lander.van.tricht@vub.be](mailto:lander.van.tricht@vub.be))*  
14

15 **Abstract.** The surface mass balance of a glacier (SMB) provides the link between the glacier and the local climate.  
16 For this reason, it is intensively studied and monitored. However, major efforts are required to determine the point  
17 SMB on a sufficient number of locations to capture the heterogeneity of the SMB pattern. Furthermore, because  
18 of the time-consuming and costly nature of these measurements, detailed SMB measurements are carried out on  
19 only a limited number of glaciers. In this study, we investigate how to accurately determine the SMB in the ablation  
20 zone of Vadret da Morteratsch and Vadret Pers (Engadin, Switzerland) using the continuity-equation method,  
21 based on the expression of conservation of mass for glacier flow with constant density. An elaborate dataset  
22 (spanning the 2017-2020 period) of high-resolution data derived from Unoccupied Aerial Vehicle (UAV)  
23 measurements (surface elevation changes and surface velocities) is combined with reconstructed ice thickness  
24 fields (based on radar measurements). To determine the performance of the method, we compare modelled SMB  
25 with measured SMB values at the position of stakes. Our results indicate that with annual UAV surveys, it is  
26 possible to obtain SMB estimates with a mean absolute error smaller than 0.5 metres of ice equivalent per year.  
27 Yet, our study demonstrates that to obtain these accuracies, it is necessary to consider the ice flow over spatial  
28 scales of several times the local ice thickness, accomplished in this study by applying an exponential decay filter.  
29 Furthermore, our study highlights the crucial importance of the ice thickness, which must be sufficiently well  
30 known in order to accurately apply the method. The latter currently seems to hamper the application of the  
31 continuity-equation method to derive detailed SMB patterns on regional to global scales.  
32  
33

## 1 Introduction

The surface mass balance of a glacier is determined by the processes adding mass to the surface (e.g. snow fall, freezing rain), and those removing mass from the surface (e.g. snow and ice melt, sublimation). These processes are strongly driven by the energy budget and precipitation over the glacier. As a result of increased global mean temperatures, SMBs are becoming increasingly negative, leading to an unprecedented shrinkage of glaciers during the last decade (Zemp et al., 2019; Wouters et al., 2019). Because of the direct link with the local climatic signal, determining the glacier surface mass balance and its distribution is crucial to monitor, understand and model the reaction of glaciers to climate change. Traditionally, a stake and snow pit network is used to determine the SMB followed by an interpolation and extrapolation to obtain the glacier mean specific mass balance (Braithwaite, 2002). This can result in large errors for glaciers where the heterogeneity of the SMB cannot be captured sufficiently by the available measurements (Zemp et al., 2013). Further, because of the time-consuming and costly nature of these measurements, detailed SMB measurements are carried out on only a limited number of glaciers.

Geodetic methods provide an alternative, and have been applied since many decades in numerous studies, to monitor mass balances for individual glaciers at local to regional scales (e.g. Brun et al., 2017; Davaze et al., 2020; Sommer et al., 2020). These methods all involve comparing digital elevation models (DEMs), mainly created using airborne and satellite data, over a given period to determine local elevation changes. These local elevation changes result from an interaction between mass balance and ice flow processes and do therefore not allow to directly determine the mass balance distribution over glaciers (Berthier and Vincent, 2012). However, having such a mass balance distribution over glaciers is of large interest, as this can be used to accurately calibrate mass balance models used in large-scale glacier modelling efforts to allow for example for an accurate calibration of mass balance gradients (Zekollari et al., 2018; Marzeion et al., 2020).

Several studies have attempted to determine patterns of SMB from surface elevation changes by implementing either mass-continuity, a kinematic boundary condition at the surface or through 3D ice flow modelling (Kääb and Funk, 1999; Gudmundsson and Bauder, 1999; Hubbard et al., 2000; Reeh et al., 2002; Nuimura et al., 2011; Vincent et al., 2016; Brun et al., 2018; Bisset et al., 2020; Wagnon et al., 2021; Miles et al., 2021). In essence, these are all based on the principle of combining surface elevation changes with the ice flux divergence. While the former can be measured directly, the latter is calculated by combining various types of measurements. Most of previous studies stumbled on the necessity, resulting from the discretization of ice flow processes and spatial resolution of the data, to smooth the input data or the ice flux divergence or to resample to much lower resolutions of several hundreds of metres. Other studies used cross-sectional flux gates to simplify the problem and calculate a uniform flux divergence across a glacier area downstream of such a flux gate or between two flux gates (Berthier and Vincent, 2012; Vincent et al., 2016). Further, a recurring drawback in previous studies attempting to detect local and small-scale variations of the SMB was the lack of satellite observations with a sufficiently high spatial and temporal resolution (Ryan et al., 2015). However, with the emergence of UAVs, it turned out to be possible to detect small scale variations at unprecedented centimetre resolution. Accordingly, several studies have been conducted to derive surface velocities from repeated UAV surveys (Immerzeel et al., 2014; Ryan et al., 2015; Kraaijenbrink et al., 2016; Rossini et al., 2018; Benoit et al., 2019) while other studies focussed on the generation

74 of surface elevation changes from multiple UAV surveys, and the comparison with stake measurements (Groos et  
75 al., 2019; Yang et al., 2020). In recent years, studies have also attempted to determine the SMB at the location of  
76 individual ablation stakes using an UAV and with measured vertical velocities (e.g. Vincent et al., 2021). However,  
77 to our knowledge, no research has yet been carried out to derive a transferable method to determine the SMB  
78 distribution over an entire ablation zone using multiannual UAV measurements. Furthermore, the optimal ways to  
79 calculate the ice flux divergence, and how to represent the spatial scales over which ice flow occurs without  
80 resampling to a much lower resolution, remain a topic of discussion.

81

82 The aim of this study consists of deriving and applying a method to determine the SMB in the entire ablation zone  
83 of two glaciers by combining UAV acquired 3D data and ice thickness measurements through the continuity-  
84 equation method. We pay particular attention to the spatial scales that need to be considered in this framework and  
85 how these influence the modelled SMB. The performance is evaluated through an in-depth comparison with  
86 measured SMB values at stakes. To allow the method to be applied for other glaciers, with different data  
87 availability, we also perform a comprehensive sensitivity analysis, from which we determine which data is crucial  
88 in the application of the method and its accuracy.

89

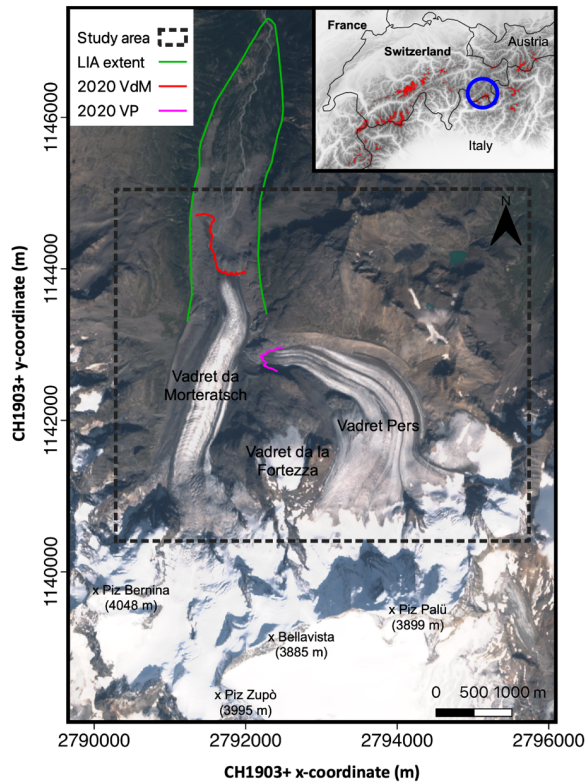
90

## 91 2 Study area and fieldwork

92

93 The current study focuses on the Morteratsch - Pers glacier complex situated in the Bernina massif in the  
94 southeastern part of Switzerland (European Alps) (Figure 1). Vadret da Morteratsch, with a current length of  
95 approximately 6 km, is the main glacier and flows from the south to the north. Vadret Pers, which flows towards  
96 Vadret da Morteratsch from the southeast, became a separate glacier in 2015, when both glaciers disconnected  
97 (Zekollari and Huybrechts, 2018). At present, the two glaciers cover an area of about 15 km<sup>2</sup> with a volume of ca.  
98 1 km<sup>3</sup> making it the largest continuous ice area in the Bernina region. Vadret da Morteratsch reached its maximum  
99 Little Ice Age (LIA) extent between 1860 and 1865 (Zekollari et al., 2014). Since 1878, the glacier front has  
100 retreated more than three kilometres and is nowadays located at an altitude of 2200 m above sea level (a.s.l.). The  
101 peculiar shape of the front of the Vadret da Morteratsch (see Figure 1) is caused by a combination of a large  
102 amount of debris on the western side that kept the ice below more insulated during the past years, and shading  
103 effects from the surrounding mountains. Since the 2000s, the front of the glacier has retreated significantly, but a  
104 large area of stagnant ice remained protruded to the north on the western side of the valley (Figure 1). The upper  
105 parts of the glacier complex reach 4000 m a.s.l, originating at peaks such as Piz Bernina and Bellavista (Figure 1)  
106 The glacier complex has been studied and monitored intensively with SMB stake measurements performed  
107 annually at the end of the ablation season since 2001 (Zekollari and Huybrechts, 2018). In addition, the geodetic  
108 mass balance of the 1980-2010 period was determined to be between -0.7 and -0.8 metres of water equivalent per  
109 year (Fischer et al., 2015). The SMB stake measurements served to calibrate a mass balance model (Nemec et al.,  
110 2009) which was coupled to a higher-order ice flow model to simulate the future evolution of the glacier complex  
111 (Zekollari et al., 2014) and to study its response time (Zekollari and Huybrechts, 2015). Furthermore, the ice  
112 thickness in the ablation area has previously been measured twice (Zekollari et al., 2013; Langhammer et al.,  
113 2019).

heeft verwijderd: and again in 2020 for specific parts of  
Vadret da Morteratsch.



116  
 117 **Figure 1.** Map of the Morteratsch-Pers glacier complex in southeastern Switzerland. The different coloured lines represent  
 118 the extent of the glacier at the end of the Little Ice Age (LIA, 1860-1865) and in 2020. The background image is a Sentinel-2  
 119 true colour composite satellite image from 13 September 2020. The highest mountains are labelled and indicated with a black  
 120 cross. The inset shows a DEM of the Shuttle Radar Topography Mission (SRTM) and boundaries of the countries of the central  
 121 and western European Alps. The areas indicated with a red colour are glaciers according to the Randolph Glacier Inventory  
 122 (RGI) version 6. The location of the Morteratsch-Pers glacier complex is indicated with a blue circle.

123

124

## 125 2.1 UAV surveys

126

127 Between 2017 and 2020, we conducted annual UAV surveys at the end of the ablation season (late September).  
 128 Hence, the focus in this research is on three mass-balance years (2017-2018, 2018-2019 and 2019-2020). In 2017,  
 129 above normal snow cover and severe weather conditions prevented drone mapping on the upper parts of the  
 130 ablation area of Vadret Pers (>2800 m) due to inadequate visual content for accurate keypoint detection (Gindraux  
 131 et al., 2017), and the inability to distribute control points. This resulted in a smaller study area in 2017-2018. The  
 132 observations consist of images acquired by repeated UAV surveys with a DJI Phantom 4 Pro (P4PRO) (in 2017,

133 2018 and 2019) and a DJI Phantom 4 RTK (P4RTK) (in 2020) quadcopter, both equipped with a 20-megapixel  
 134 camera. For flight planning and UAV piloting, DJI GS Pro was used. The flight plans were designed to limit the  
 135 variation in ground sampling distance (GSD) by flying parallel to the main surface slope and by subdividing the  
 136 study area into smaller sections. We ensured in every case sufficient overlap between the different flight plans so  
 137 that they could be easily attached to each other afterwards. Additional technical details of the flights are given in  
 138 [Table 1](#). The different flights within one field campaign were performed on multiple days. However, because of  
 139 the short fieldwork periods (4-6 days), the difference between the SMB measurements and surface elevation  
 140 changes caused by not surveying simultaneously is estimated to be at most up to 10 centimetres, which is within  
 141 the uncertainty bounds of the measurements. Therefore, no correction was applied for the difference in acquisition  
 142 dates.

143  
144

145 **Table 1.** *Technical details and characteristics of the UAV flights.*

146

Setting / characteristic	Value
<b>Flight height above the surface</b>	On average 180 m
<b>Ground resolution</b>	0.05-0.09 m
<b>View angle</b>	90°
<b>Flight speed</b>	5 m/s
<b>Capture interval</b>	4 s
<b>Frontal overlap</b>	90%
<b>Side overlap</b>	70%
<b>Survey area (2020)</b>	14.5 km <sup>2</sup>
<b>Number of images (2020)</b>	8107
<b>Average number of keypoints / image</b>	65000-70000
<b>Average matched keypoints / image</b>	32000-36000

147  
148

149 To ensure sufficient horizontal and vertical accuracy, ground control points (GCPs) were distributed over the area  
 150 of interest (see Figure 2). The GCPs, plastic orange squares of 40x40 cm, were measured with a Trimble 7 GeoXH  
 151 RTK GPS (horizontal average accuracy of 10-20 cm, vertical average accuracy of 20-30 cm) by relying on the  
 152 Swiss Positioning Service (swipos) GIS/GEO. The GCPs were spread over different locations on the glacier  
 153 following density and distribution guidelines from the literature (Tahar et al., 2012; Goldstein et al., 2015; Long  
 154 et al., 2016; Tonkin et al., 2016; Gindraux et al., 2017). We ensured homogeneous distribution in almost every  
 155 case, except where crevasses, moulins or a fresh layer of snow (especially in 2017) impeded this with an average  
 156 density of 10-20 GCPs km<sup>-2</sup>. Specific attention was paid to the distribution of GCPs in the overlapping areas of  
 157 the different flight areas in order to be able to georeference two neighbouring flight areas with the same points. In  
 158 2020, a smaller number of GCPs was placed because the P4RTK can achieve centimetre-level accuracy without a  
 159 large number of GCPs as a result of an on-board differential GPS system (Zhang et al., 2019; Kienholz et al.,  
 160 2020). Each year, some of the GCPs were not used for the georeferencing process, but as a ground validation point  
 161 (GVP) to assess the quality of the reconstructed DSM.

162

heeft opmaak toegepast: Lettertype: 10 pt, Niet Cursief

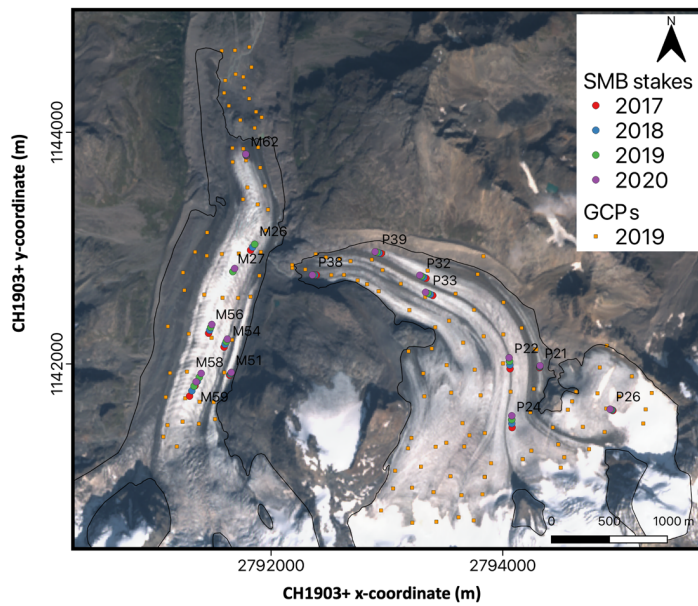
heeft verwijderd: Table 1

heeft verwijderd: (typically 20%)

165  
166  
167  
168  
169  
170  
171  
172  
173  
174  
175  
176  
177  
178  
179

## 2.2 In situ surface mass balance data

A total of 287 annual mass balance stake measurements (158 on Morteratsch, 129 on Pers) were performed between 2001 and 2020 in the ablation area of the glacier complex, with an average number of 15 stakes in each year. All the stakes were located between 2100 and 2600 m a.s.l. on the Morteratsch glacier's ablation tongue and between 2450 and 3050 (approximately the ELA) on Vadret Pers. Zekollari and Huybrechts (2018) summarized these measurements and found the SMB rate on Pers glacier to be significantly lower (-2.1 to -2.5 metres of ice equivalent (m i.e.) yr<sup>-1</sup>) compared to Vadret da Morteratsch at similar elevation. This has been mainly attributed to differences in orientation and the associated daily insolation cycle over the two glaciers. For the period of concern in this study (2017-2020), SMB measurements from 16 individual stakes (8 on each glacier) are available for every year on the debris-free part of the ablation areas (Figure 2). The stakes were measured, and replaced if necessary, annually at the end of each ablation season, during the UAV surveys.



180  
181  
182  
183  
184  
185  
186  
187

**Figure 2.** Satellite image of the study area with the location of the measured ablation stakes in 2017, 2018, 2019 and 2020. The GCPs of 2019 are indicated with an orange square. The background image is a Sentinel-2 true colour composite satellite image from 13 September 2020. The different locations of the stakes in 2017-2018-2019-2020 show the movement of the stakes with the glacier flow. The labels refer to the stake names as used in the fieldwork programme. In 2019, stake M26, which was located in the middle of a crevasse field, was replaced by stake M27.

188

### 189 2.3 Ice thickness data

190

191 To calculate the local ice volume flux divergence (see section 3.4), a distribution of the ice thickness is required.  
192 There are two published datasets of the ice thickness of the Morteratsch – Pers glacier complex, derived from radar  
193 measurements (especially in the ablation area) and modelling (especially in the accumulation area). The first one  
194 is the dataset of Zekollari et al. (2013), hereafter referred to as THIZ. This distribution was reconstructed by  
195 combining measured ice thicknesses (~30 ground borne GPR profiles in the early 2000s) with different modelling  
196 constraints. The second ice thickness distribution is the dataset of Langhammer et al. (2019), hereafter referred to  
197 as THIL. This distribution was produced by combining measured ice thicknesses (41 helicopter borne GPR profiles  
198 with a total of 53247 points measured in 2017) and modelling constraints with the Glacier Thickness Estimation  
199 (GlaTE) inversion scheme (Langhammer et al., 2019). We correct both datasets for glacier geometry changes to  
200 refer to the glacier state in 2018, 2019 and 2020 respectively by subtracting the amount of local surface lowering.  
201 This concerns the local height difference between the UAV created DSMs of 2018-2019-2020 and the DEM used  
202 for the respective ice thickness datasets. The latter are two DEMs provided by SwissTopo. DHM25 valid for 1991  
203 (used for THIZ) and SwissALTI3D valid for 2015 (used for THIL).

204

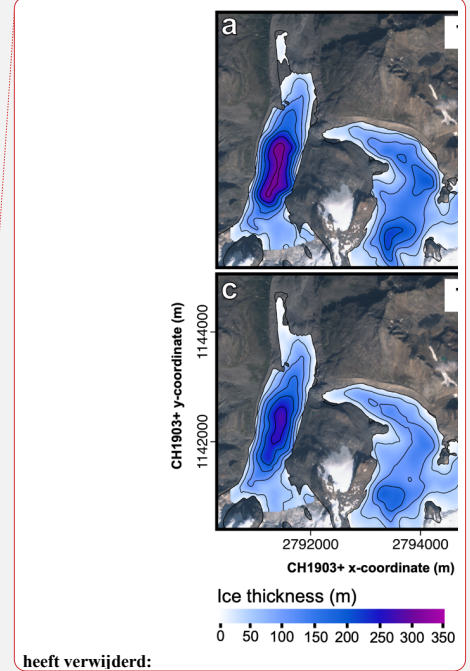
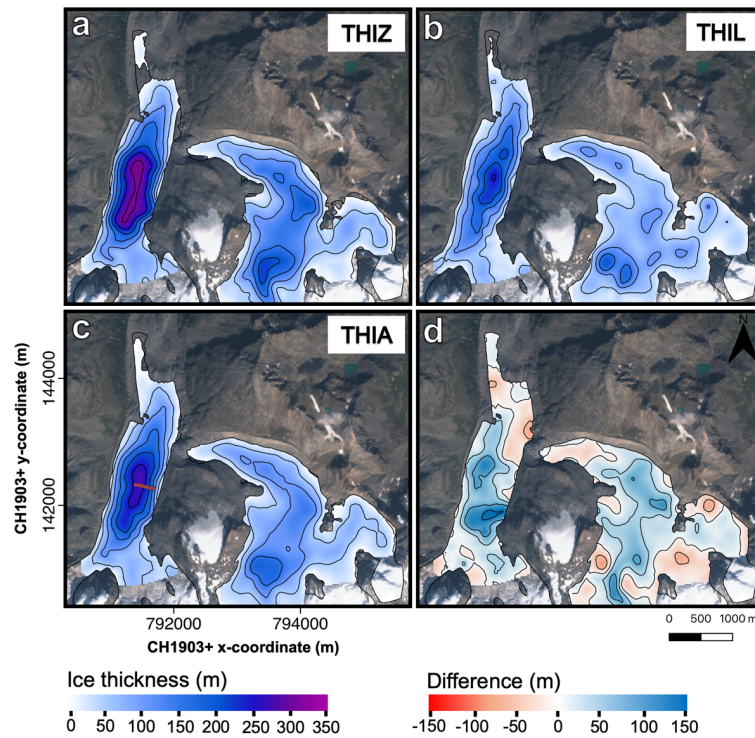
205 Although both ice thickness distributions (Figure 3a and Figure 3b) have a similar pattern (location of  
206 overdeepenings, location of maximum ice thickness), large local differences exist (Figure 3d). The ice thickness  
207 maximum, corrected to represent the ice thickness in 2020, for instance occurs at a similar location but is about  
208 310 m for THIZ and 250 m for THIL. This corresponds to a difference of 18-24% which is however still within  
209 the error bounds of the datasets. Conversely, there are also certain zones (especially higher up Vadret da  
210 Morteratsch) where the difference between the two datasets is about 150 metres.

211

212 Because of the significant differences between both ice thickness distributions, the choice for a particular  
213 distribution has a considerable effect for the calculations in this study. To verify the maximum ice thickness of  
214 Vadret da Morteratsch, we measured the ice thickness once again in the thickest region in 2020 (see Figure 3c)  
215 with a Narod Radio Echo Sounding (RES) system, similar to Zekollari et al. (2013) and Van Tricht et al. (2021).  
216 We preferred to use a low frequency of 5 MHz to limit the amount of attenuation due to disturbances in the glacier  
217 such as water inclusions, repeatedly observed during the fieldwork. We found a maximum value of 296 metres  
218 which is relatively close to the maximum thickness from the THIZ dataset. We can therefore certainly not ignore  
219 this dataset, despite the smaller number of measurements and the older date of creation. Therefore, for further  
220 calculations, we decided to use the mean ice thickness from THIZ and THIL at every grid cell, hereafter referred  
221 to as THIA (Figure 3c). The effect of using THIA, as opposed to relying on THIZ or THIL, is examined as a part  
222 of the sensitivity analysis (see section 5.1). For the areas where the current elevation is lower than the bedrock  
223 inferred from THIZ and THIL, and where there is no ice as a result within the current glacier outline, we assume  
224 a minimal ice thickness of 5 m as in Zekollari et al. (2013).

225

226



227

228 **Figure 3.** Ice thickness distribution of the ablation area of the Morteratsch-Pers glacier complex in 2020. (a) THIZ (ice  
 229 thickness distribution of Zekollari et al. (2013), (b) THIL (ice thickness distribution of Langhammer et al. (2019) and (c) THIA  
 230 (average ice thickness distribution). The difference between THIZ and THIL is shown in panel d. Contour lines represent 50 m  
 231 intervals. Note that at the front of Vadret da Morteratsch and locally at the front of Vadret Pers, the glacier outline is larger  
 232 than the ice thickness dataset. The current surface elevation of these areas is lower than the bedrock elevation inferred from  
 233 THIL and THIZ. *The locations of the ice thickness measurements of 2020 are added in panel c with red circles.* The background  
 234 image is a Sentinel-2 true colour composite satellite image from 13 September 2020.

235

236

### 237 3 Methods

238

#### 239 3.1 Continuity-equation method

240

241 The continuity equation for glacier flow with constant density (Eq. 1) links the local mass balance ( $b$ ) and the ice  
 242 flux divergence per unit width in the local vertical ice column ( $\nabla \cdot \mathbf{q}$ ) with local changes in the ice thickness ( $\frac{\partial H}{\partial t}$ ),  
 243 all expressed in  $\text{m i.e. yr}^{-1}$  (see e.g. Hubbard et al., 2000; Berthier and Vincent, 2012).

244

246

$$\frac{\partial H}{\partial t} = b - \nabla \cdot \mathbf{q} \quad (1)$$

248

249

Eq. 1 shows that the difference between the local mass balance and ice flux divergence must be compensated by a change in local ice thickness. If the bedrock elevation is assumed to be constant and compaction is negligible, which is the case in the ablation area (with ice throughout the entire column), the local ice thickness (H) in Eq. 1 can be replaced by the elevation of the surface (h). Further, because basal and internal mass balance in the ablation area are predominantly much smaller compared to the surface mass balance ( $b_s$ ) (Kaser et al., 2003; Huss et al., 2015), b can be replaced by  $b_s$ , which after a reorganisation leads to the following expression:

256

257

$$b_s = \frac{\partial h}{\partial t} + \nabla \cdot \mathbf{q} \quad (2)$$

259

260

By determining the local elevation changes (section 3.2) and the components that make up for the ice flux divergence per unit width (from now on referred to as ice flux divergence; sections 3.3-3.4), the SMB pattern can then be derived.

264

265

### 3.2 DSM generation and surface elevation changes ( $\partial h/\partial t$ )

267

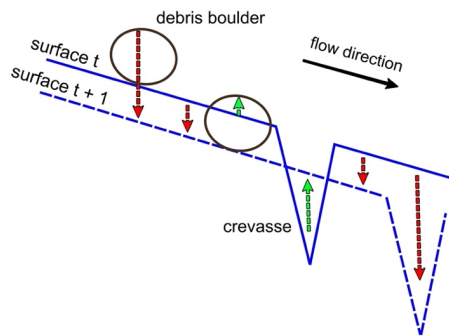
First, all the data from the UAV surveys are used to generate DSMs on a common local coordinate system (CH1903+ LV95). All the images collected during the UAV surveys are processed into orthophotos and DSMs using the photogrammetry workflow implemented in Pix4D. The accuracy of the reconstructed DSMs is assessed using the GVPs and the stable terrain outside the glacierized areas. Subsequently, surface elevation changes are directly computed from these DSMs by subtracting the DSMs from each other (2018-2017, 2019-2018, 2020-2019). Initially, all the DSMs are generated with a very high resolution of 0.05-0.09 m. But eventually, the surface elevation changes are resampled to 25 m resolution for further calculations using a block moving average filter. This corresponds to the resolution of the ice thickness datasets and will therefore be the grid size for all of the following calculations.

277

A commonly observed feature on surface elevation change maps derived from high resolution DSMs are alternating positive and negative differences. These are caused by the advection of local glacier topography such as crevasses, moulins, supraglacial melt streams, and large ice or rock boulders (Figure 4) (Brun et al., 2018; Rounce et al., 2018; Yang et al., 2020). The above-mentioned variations are not caused by reduced or increased melt or accumulation and therefore need to be corrected for ice flow to make a correct SMB estimate.

283

284



285  
286  
287  
288  
289  
290  
291

**Figure 4.** The advection of surface topography (such as debris boulders and crevasses) can alter surface elevation changes between timestep  $t$  and  $t+1$  (red = negative  $\partial h/\partial t$ , green = positive  $\partial h/\partial t$ ). The net effect on the surface elevation depends on the amount of lowering and the vertical extent of the moving features on the glacier surface.

292 The different DSMs are treated considering the motion of the ice, following the method applied in e.g. Brun et al. (2018). This method consists of projecting each point on the glacier back to its original position in the previous year, based on the local velocity in x and y direction and taking into account the vertical displacement produced by flow along the longitudinal slope. The latter is determined by taking the average slope over all the different years for which a DSM was made, smoothed with a Gaussian filter.

297  
298

### 3.3 Horizontal surface velocity

300

301 Glacier surface velocities, which are needed to calculate the ice flux divergence (section 3.4) and to flow correct the surface elevation changes (section 3.2), are computed for the three individual mass balance years. Velocity grids are derived by applying the Image Geo Rectification and Feature Tracking toolbox (ImGRAFT), an open-source tool in MATLAB (Messerli and Grinsted, 2015). Specific settings for the template matching of ImGRAFT are the use of the orientation correlation (OC) method and a large search height and search width of 200 m, to guarantee that all possible areas are covered. Instead of using visual image data with variable illumination and snow cover, the feature tracking algorithm is run on hillshades (relief DSMs) of the original DSMs resampled to a resolution of 2 m (Messerli and Grinsted, 2015). The latter turned out to improve the correlation success (Rounce et al., 2018).

310

311 Velocity maps are computed and corrected for differences in acquisition dates to obtain values in metre per year. Then, a series of filters is applied to the output of the cross-correlation to exclude poorly correlated pixels and those with unrealistic displacements or flow directions (Ruiz et al., 2015). The latter is a common issue for snow

313

314 covered areas, debris covered areas or complex crevasses areas where no accurate displacements can be detected.  
 315 As a first filter, after verifying average zero displacement for stable areas outside the glacier, all the computed  
 316 velocity vectors outside the glacierized areas are removed by using the digitized glacier outlines (Heid and Kääb,  
 317 2012). The latter are manually digitized based on drone and satellite images and correspond to the end of the  
 318 summer of every balance year under consideration. Then, a median filter is applied which removes velocity  
 319 components that deviate too much from the surrounding vectors (Heid and Kääb, 2012; Nagy et al., 2019). Finally,  
 320 we also impose a maximum velocity threshold derived from the modelled velocities in Zekollari et al. (2013),  
 321 which are constrained with field observations. In other words, we limit the maximum surface velocity at every  
 322 grid cell to the velocity modelled in Zekollari et al. (2013) + 20%. The latter is a margin to take into account  
 323 potential errors present in the study of Zekollari et al. (2013). However, after analysis this proved not to be  
 324 necessary as these high values did not occur. The raw velocity maps containing gaps after filtering are then  
 325 interpolated using a cubic spline interpolation (Ruiz et al., 2015). As validation, we compare the obtained velocities  
 326 with measured velocities from stakes.

327

328

#### 329 **3.4. Ice flux divergence from ice thickness and surface velocities**

330

331 The ice flux divergence (in m i.e. yr<sup>-1</sup>) corresponds to the local upward or downward flow of ice relative to the  
 332 glacier surface. It represents the difference between the ice supplied from upstream and lost downstream at a  
 333 particular position. It is defined to be negative for upward motion (mass supplied to the surface, also referred to as  
 334 the emergence velocity) and positive for downward motion (mass is removed from the surface, also referred to as  
 335 the submergence velocity).

336

337 Different approaches exist to calculate the ice flux divergence ranging from the use of 3D ice flow models  
 338 (Seroussi et al., 2011; Vincent et al., 2021) to the use of simple geometric calculations and flux gates (Nuimura et  
 339 al., 2011; Berthier and Vincent, 2012). The important distinction is the simplicity and the resolution with which  
 340 they can be calculated. In this study, the ice flux divergence is computed for each grid cell, by combining surface  
 341 velocities and ice thickness according to Eq. 3:

342

343

$$344 \nabla \cdot \mathbf{q} = F \left( u_{s,x} \frac{\partial H}{\partial x} + u_{s,y} \frac{\partial H}{\partial y} + H \frac{\partial u_{s,x}}{\partial x} + H \frac{\partial u_{s,y}}{\partial y} \right) \quad (3)$$

345

346

347 The right side of Eq. 3 contains two horizontal ice flux components of which the first corresponds to the ice  
 348 thickness divergence and the second one to the velocity divergence (Reeh et al., 2003). Both are computed from  
 349 the relevant derivatives. F is the depth averaged glacier velocity ratio ( $\bar{u}/u_s$ ). For an isothermal glacier, with  
 350 negligible basal sliding and Glen's flow coefficient  $n = 3$ , F is 0.8. However, the Morteratsch-Pers glacier complex  
 351 is assumed to be a temperate alpine glacier complex which is accompanied by basal sliding. According to Zekollari  
 352 et al. (2013), internal deformation accounts glacier wide on average for 70% of the flow and basal sliding for the  
 353 remaining 30%. However, in the ablation area the contribution of internal deformation is most likely even higher.

354 Therefore, for the standard runs in this study, we take an F-value of 0.9. However, the F-value may vary locally  
355 (Zekollari et al., 2013) and varying this parameter will therefore be part of the sensitivity analysis.

356

357

### 358 **3.5. Spatial scales of the ice flux divergence**

359

360 In contrast to the surface elevation changes, for which the accuracy is expected to be high, the computed ice flux  
361 divergence is subject to larger uncertainties. This uncertainty directly relates to the large uncertainties in the  
362 reconstructed ice thickness field. Moreover, a considerable part of the uncertainty also originates from the spatial  
363 scales that need to be considered: due to longitudinal stresses, the local ice dynamics do not only depend on the  
364 local glacier geometry (an assumption of the Shallow Ice Approximation, see e.g. Hutter and Morland (1984)),  
365 but also on the surrounding geometry, typically over scales corresponding to several times the local ice thickness  
366 (accounted for in higher-order and Full Stokes models, see e.g. Zekollari et al. (2014), where such a model was  
367 applied for this glacier complex). Local gradients of the ice thickness and the velocity are often magnified when  
368 they are determined on a numerical grid with a central difference scheme. This is directly reflected in the ice flux  
369 divergence pattern. Therefore, to make the ice flux divergence solution independent of the resolution and to take  
370 non-local stresses into account, larger scales must be considered (Reeh et al., 2003; Rounce et al., 2018). To date,  
371 studies applying the continuity equation method, usually resampled the ice flux divergence grid to a much lower  
372 resolution (Nuimura et al., 2011; Seroussi et al., 2011; Rounce et al., 2018) or considered a flux gate approach  
373 (Berthier and Vincent., 2012; Vincent et al., 2016; Brun et al., 2018). However, as we aim for a high resolution of  
374 the SMB determination in this study and to obtain spatial variations in the ice flux divergence field, we opt to  
375 retain the 25 m resolution and to apply a filter to consider larger scales for the calculation of the ice flux divergence.

376

377 Different filters have been applied, of which most are constant box filters (e.g. mean, median) with a strong  
378 variation in size (up to 10000 metres) (Kääb and Funk, 1999; Seroussi et al., 2011; Rounce et al., 2018). Such  
379 filters give equal weights to cells within the box irrespective of their distance from the point in consideration  
380 (Kamb and Echelmeyer, 1986; Le Brocq et al., 2006). In this way, the effects of local phenomena (such as an ice  
381 fall or an acceleration in the glacier flow) are spread out uniformly when these filters are applied over larger  
382 distances, which implies that there are no localized peaks in the flux divergence field. Also, these filters have an  
383 abrupt cut-off point where the weighting becomes zero (Le Brocq et al., 2006). Furthermore, effects of  
384 perturbations in for example ice thickness have been demonstrated to fade out exponentially for ice flow (Kamb  
385 and Echelmeyer, 1986). Because of all these reasons, we apply in this study a local exponential decay filter (Eq.  
386 4):

387

388

$$389 \nabla \cdot \mathbf{q}_{[x,y]} = \sum_{i=-\text{dist}}^{\text{dist}} \sum_{j=-\text{dist}}^{\text{dist}} W_{[x+i,y+j]} \nabla \cdot \mathbf{q}_{[x+i,y+j]} \quad (4)$$

390

391

392 In Eq. 4, dist is the maximum distance of a cell which is taken into account in the exponential decay filter (set at  
393 2.5 km), i and j are indices, and W represents the weight of a particular cell at position [x+i, y+j] (Le Brocq et al.,  
394 2006):

$$397 W_{[x,y]} = e^{-\frac{1}{sl} \sqrt{(x'-x)^2 + (y'-y)^2}} \quad (5)$$

398  
399 In Eq. 5, x and y are the coordinates of the point being filtered while x' and y' are the coordinates of the weighted  
400 points, sl is the scaling length and is a crucial parameter determining how fast the exponential filter fades. This  
401 parameter directly relates to the length scale over which the longitudinal stresses determine the local ice flow.  
402 Theoretically, this scaling length is in the range of 1-3 times the local ice thickness for valley glaciers and 4-10  
403 times for ice sheets (Kamb and Echelmeyer, 1986; Le Brocq et al., 2006). For our experiments, we vary the scaling  
404 length depending on A times the local ice thickness (Eq. 6). In this way, we incorporate variations within the study  
405 area into the exponential decay filter and we account for non-local flow coupling. The latter was shown to be an  
406 improvement compared to fixed-size filters (Le Brocq et al., 2006). In this way, the ice flux divergence in areas  
407 with a larger ice thickness is considered over a larger distance compared to areas with a smaller ice thickness.  
408

$$409 \quad 410 \quad 411 \quad 412 \quad 413 \quad 414 \quad 415 \quad 416 \quad 417 \quad 418 \quad 419 \quad 420 \quad 421 \quad 422 \quad 423 \quad 424 \quad 425 \quad 426 \quad 427 \quad 428 \quad 429 \quad 430$$
$$sl[x,y] = A * H[x,y] \text{ with } A \in \{0:1:10\} \quad (6)$$

To provide for conservation of mass, the filtered result in each grid cell is multiplied by the ratio of the net flux  
divergence (sum of all ice flux divergences) before and after filtering. To determine the optimal procedure to  
include the effects of (longitudinal) stresses and uncertainty in the input data, we perform multiple experiments  
with the exponential decay filter. For this, we examine whether (i) the ice flux divergence, (ii) the gradients of  
velocity and ice thickness or (iii) both should be considered over larger spatial scales for optimal results in the  
determination of the SMB.

First, the ice flux divergence is considered over larger spatial scales by applying the exponential decay filter to the  
ice flux divergence field. Second, to compensate solely for the effects of large gradients, the gradients are  
considered over larger spatial scales. We therefore apply the exponential filter to the ice thickness and velocity  
gradients and calculate the ice flux divergence using these smoothed gradients. Third, to compensate for the  
negative effects of very large scaling lengths for both previous experiments and the biases related to both, we filter  
twice. Hence, both filters are applied after each other. In this way, the smoothness of the ice flux divergence field  
increases while the top values are not damped as much as applying a filter once with a long scaling length. This  
tends to reduce the distance over which the filtering must be performed, which is favourable to preserve local  
variations.

431 For every experiment, the modelled and measured SMB values at the position of the stakes are compared (see  
 432 section 2.2). As metrics to quantify the performance of the procedure, the mean absolute error (MAE) and the root  
 433 mean square error (RMSE) are used (Eq. 7 and 8). The MAE is defined as the absolute difference between the  
 434 modelled and the measured SMB. The RMSE on the other hand takes into account the variance of the errors. n is  
 435 the number of stake measurements. The uncertainty of the SMB measurements is estimated to be  $\pm 0.2$  m i.e yr<sup>-1</sup>  
 436 and is also considered in the analysis. More specifically, for each filter option we carry out 100 versions in which  
 437 we perturb the measured SMB. This is done by randomly adding a value between -0.2 and 0.2 distributed around  
 438 0. Then, for the option under consideration, the average MAE and RMSE are calculated from Eqs. 7 and 8, where  
 439 n is the number of SMB measurements for every year, see section 2.2. i is an index ranging from 1 to n (16), x<sub>i</sub>  
 440 and y<sub>i</sub> are the Cartesian coordinates of the different stakes under consideration.

441  
 442

$$443 \text{ MAE} = \frac{1}{n} \left( \left| \sum_{i=1}^n b_{s,\text{modelled}}(x_i, y_i) - b_{s,\text{measured}}(i) \right| \right) \quad (7)$$

444

$$445 \text{ RMSE} = \sqrt{\frac{\sum_{i=1}^n (b_{s,\text{modelled}}(x_i, y_i) - b_{s,\text{measured}}(i))^2}{n}} \quad (8)$$

446

447

## 448 4 Results

449

### 450 4.1 Surface elevation changes and filtering

451

452 The accuracy of the elevation product is first assessed by comparing the photogrammetrically created DSMs with  
 453 GVPs, randomly divided over the study area. MAE between measured and modelled elevation are in the order of  
 454 a few cm (Table 2), which is similar to values found in other studies (Whitehead et al., 2013; Immerzeel et al.,  
 455 2014; Wigmore and Mark, 2017; Zhang et al., 2019). As such, the accuracy of the created DSMs is high.  
 456 Furthermore, the mean error (ME) is close to zero which indicates that the created DSMs are not biased. For 2017,  
 457 the slightly larger MAE is probably caused by a smaller number of GCPs combined with a reduced visual content  
 458 because of fresh snow on the glacier surface. Further, the small MAE and RMSE of the DSM in 2020 highlight  
 459 the advantage of using a RTK equipped with an RTK GPS (P4RTK) for which a smaller amount of GCPs is needed  
 460 to reach similar or better accuracies compared to a classic setup (UAV without RTK correction).

461

462

463

464

465

466

467

heeft verwijderd: Mean absolute errors (

heeft verwijderd: )

470 **Table 2.** Mean absolute error (MAE), mean error (ME), and root mean square error (RMSE) of the elevation differences  
 471 between the DSMs and the GVPs in different years. (Units are in m i.e.). The GCP density is the number of GCPs per square  
 472 kilometre while the column of GVPs represents the total number of GVPs in each year.

Year	MAE	ME	RMSE	GCP density (km <sup>-2</sup> )	GVPs	UAV used
2017	0.09	-0.07	0.16	11	10	P4PRO
2018	0.06	-0.02	0.22	24	34	P4PRO
2019	0.08	0.03	0.16	18	27	P4PRO
2020	0.07	0.03	0.10	11	19	P4RTK

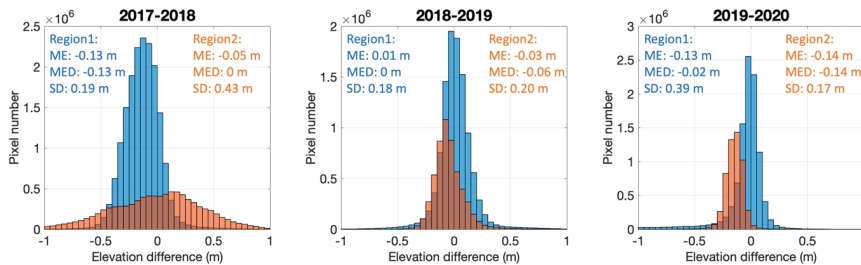
heeft verwijderd: Mean absolute error (MAE) and root mean square error (RMSE) of the elevation differences between the DSMs and the GVPs in different years. (Units are in m i.e.).

Tabel met opmaak

474  
 475  
 476 Then, the accuracy of the surface elevation changes is assessed by comparing the elevation differences in  
 477 rectangular areas outside the glacierized areas for two regions (see Figure 6), where the topography is assumed to  
 478 be mostly stable (Yang et al., 2020). The histograms for the three different balance years in consideration show  
 479 that most of the differences range between -0.2 and 0.2 m, which indicates that there is no large absolute offset  
 480 between the DSMs of the different years (Figure 5). For region 2, we find a larger standard deviation (SD) for the  
 481 2017-2018 difference which appears to be caused by a small horizontal shift which produces larger elevation  
 482 differences (both negative and positive) in this steeper area. For the gentler sloping glacier surface, the effects are  
 483 negligible. The larger SD for the 2019-2020 difference in region 1 is caused by an area where a part of the bare  
 484 surface was eroded by a melt river, producing a tail of negative elevation differences. In general, the above analysis  
 485 reveals that the vertical uncertainties resulting from the DSM differencing are limited.

heeft verwijderd: Figure 6

heeft opmaak toegepast: Lettertype: 10 pt, Niet Cursief, Engels (Groot-Brittannië)

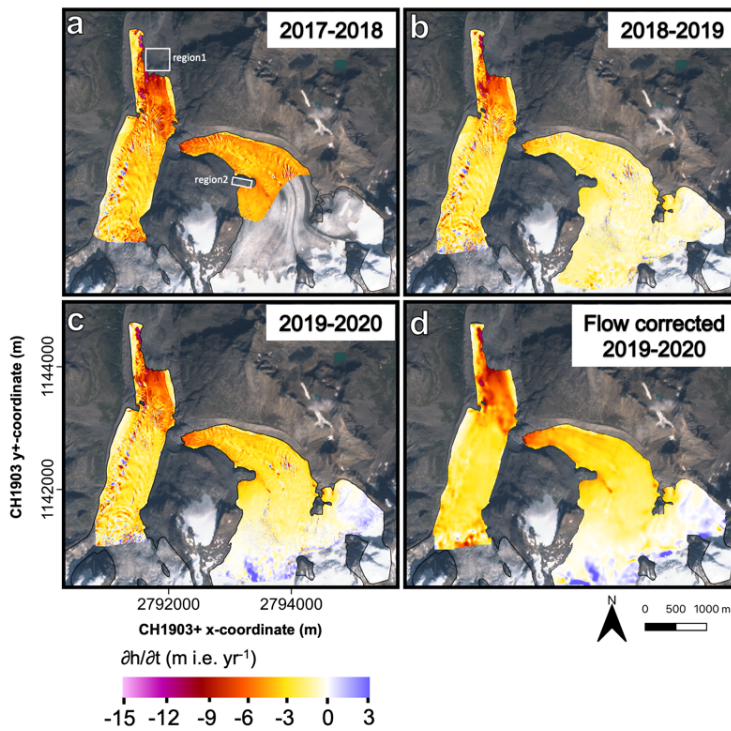


488  
 489 **Figure 5.** Histograms of elevation differences for the different balance years considered. The mean error (ME), median error (MED), and standard deviation (SD) are added for each region.

492  
 493  
 494 The different maps for the three balance years, display a very detailed pattern of surface elevation changes (Figure  
 495 6). For example, alternating positive and negative surface elevation changes are noticeable and can be explained  
 496 by the advection of local glacier surface topography due to glacier movement (see also Figure 4). In addition,  
 497 significant less negative  $\partial h/\partial t$  values at the left side of Vadret da Morteratsch, especially where the glacier

503 protrudes towards the north, are likely the result of a debris cover insulating the ice below and decreasing the  
 504 melting rate (Reznichenko et al., 2010; Rounce et al., 2018; Rossini et al., 2018). The latter was also observed by  
 505 the study of Rossini et al. (2018) focussing on the elevation differences on the front of Vadret da Morteratsch in  
 506 the summer of 2016. Only at the terminal ice cliff, significantly higher  $\partial h/\partial t$  values can be observed (Immerzeel  
 507 et al., 2014). Given that the ice fluxes can be assumed to remain relatively constant over the three years in  
 508 consideration, the elevation changes indicate that 2017-2018 was the year with the most negative SMB (which is  
 509 confirmed by field measurements (see Figure 11). Further, large positive surface elevation changes can be  
 510 distinguished for 2019-2020 at the highest part of Vadret Pers. This is probably the result of avalanches originating  
 511 from the steep accumulation area and persistent snow cover in these areas. This is striking as surface elevation  
 512 changes further down on the glacier are generally more negative compared to 2018-2019: i.e. the SMB gradient  
 513 on Vadret Pers is steeper in 2019-2020 compared to 2018-2019.

514  
 515



516  
 517

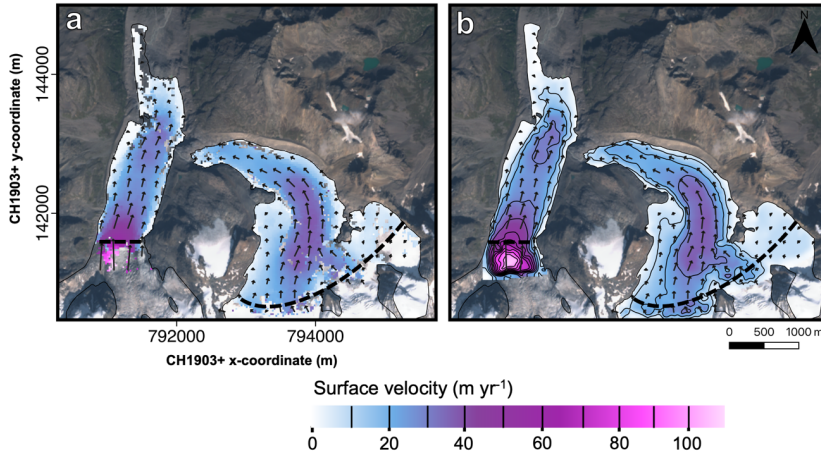
518 **Figure 6.** Surface elevation changes for (a) 2017-2018, (b) 2018-2019 and (c) 2019-2020. The spatial resolution is equal to 8  
 519 cm. Panel d shows the surface elevation changes for 2019-2020 after flow correction. The outline of the glacier corresponds  
 520 to the latest year of observation for every balance year in consideration. The two white boxes (region 1 and region 2) are stable  
 521 areas which are used for the error analysis. The background image is a Sentinel-2 true colour composite satellite image from  
 522 13 September 2020.

523  
524  
525  
526  
527  
528  
529  
530  
531  
532  
533  
534  
535  
536  
537  
538  
539  
540  
541

Alternating positive and negative surface elevation changes are occurring, caused by the advection of surface topography (Figure 4 and Figure 6). We correct for these non-SMB features by flow correcting the DSMs (see section 3.2). The alternating pattern has clearly faded (Figure 6d). At the top of the ablation area of Vadret da Morteratsch, near the ice fall, the  $\partial h/\partial t$  values at the margin of the area are unrealistic because of inaccurate velocity calculations (see Figure ) and margin effects of the longitudinal slope. However, this area lies outside the area under investigation (see Figure ).

#### 4.2 Glacier surface velocity

The velocity map derived from feature tracking and filtered for errors (see section 3.3), contains several voids (Figure 7a). This is caused by a lack of correlation between the two years, which is typically related to deformations of the surface, repositioning of supraglacial melt streams, and the presence of snow cover or debris. The latter hampers an accurate tracking between two consecutive years. To fill these gaps, cubic spline interpolation is used (Figure 7b).



542  
543  
544  
545  
546  
547  
548  
549

**Figure 7.** Horizontal surface velocities derived from feature tracking between 2019 and 2020. (a) filtered surface velocity, (b) void-filled filtered surface velocity. The black arrows indicate the flow direction. The dashed black line indicates the limit of the glacier area where the velocity is modelled without many gaps (area used for further analyses, e.g. when calculating ice flux divergences). The background image is a Sentinel-2 true colour composite satellite image from 13 September 2020. The contour lines are added for every 10 m and they are indicated in the colorbar.

heeft verwijderd: Figure 6

heeft opmaak toegepast: Lettertype: 10 pt, Niet Cursief, Engels (Groot-Brittannië)

heeft verwijderd: Figure

heeft opmaak toegepast: Lettertype: 10 pt, Niet Vet, Niet Cursief, Engels (Groot-Brittannië)

heeft opmaak toegepast: Lettertype: 10 pt, Niet Vet, Niet Cursief, Engels (Groot-Brittannië)

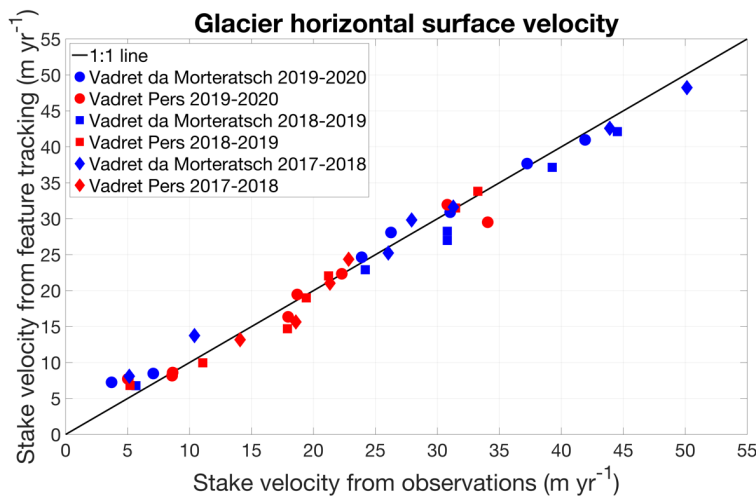
heeft verwijderd: Figure

553

554 Comparison with the velocities obtained by field measurements using ablation stakes (based on high-precision  
555 RTK GPS system, estimated accuracy of approx.  $0.1 \text{ m yr}^{-1}$ ) reveals a good agreement. We find the ME and RMSE  
556 to be  $0.01 / 1.7 \text{ m yr}^{-1}$  for 2017-2018,  $0.99 / 1.9 \text{ m yr}^{-1}$  for 2018-2019 and  $-0.37 / 1.8 \text{ m yr}^{-1}$  for 2019-2020 (Figure  
557 8).

558

559



560

561

562 **Figure 8.** Comparison between surface velocities at stakes from field observations (high precision GPS measurement at stakes)  
563 and from feature tracking.

564

565

566 The surface velocities of 2017-2018 are higher compared to 2018-2019. Because the surface velocities in 2019-  
567 2020 also appear to be slightly larger compared to 2018-2019, it might be due to a larger amount of basal sliding  
568 in these two balance years. The latter can be caused by an increased supply of meltwater lubricating the glacier's  
569 base which can be linked to a more negative  $\partial h/\partial t$  in 2017-2018 and 2019-2020 compared to 2018-2019 (see also  
570 Figure 6).

571

572

### 573 4.3 Ice flux divergence

574

575 After considering various spatial scales and filter procedures to determine the ice flux divergence, we find optimal  
576 results (lowest MAE, RMSE and minimal scaling length, see section 5.2) when both filters are applied after each  
577 other for a scaling length of  $4xH$  to smooth the ice thickness and velocity gradients and a scaling length of  $1xH$  to  
578 smooth the ensuing ice flux divergence (see section 3.5). These values are close to the theoretical values of the

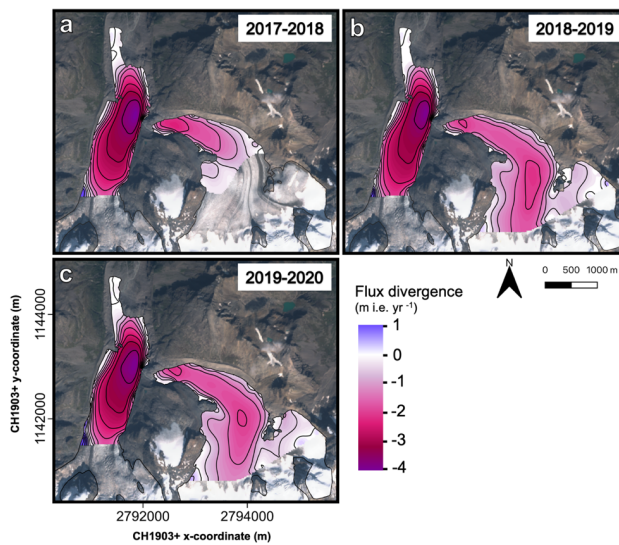
579 fundamental longitudinal scaling length for valley glaciers, mentioned in Kamb and Echelmeyer (1986). It shows  
580 that the data needs to be considered over large spatial scales which implies that the ice flux divergence field must  
581 be sufficiently smooth to give accurate results.

582

583 The computed ice flux divergence is clearly characterized by negative values over both glacier tongues (Figure 9).  
584 This represents horizontal compression and associated vertical extension which is generally expected for ablation  
585 areas (e.g. Kääh and Funk, 1999). This horizontal compression translates into an ice supply towards the surface  
586 (emergence velocity), which counters the effect of the negative mass balance on the local ice thickness change  
587 (and neutralizes it in case the glacier is in equilibrium with the local climatic conditions). The ice flux divergence  
588 reaches a minimum between 500 and 1000 m from the terminus of the Vadret da Morteratsch with values close to  
589  $-4$  m i.e.  $\text{yr}^{-1}$  (Figure 9). In this area, both the ice thickness (Figure 3) and the surface velocity (Figure 7) decrease  
590 significantly which leads to large negative gradients and hence upward motion (negative ice flux divergence). It  
591 is therefore not surprising that there is a complex pattern of transverse crevasses in this area (see Figure 2). The  
592 maximum ice flux divergence at the eastern side of Vadret da Morteratsch near the former confluence area with  
593 Vadret Pers is suspicious. This is likely caused by the very large ice thickness gradient because of the contribution  
594 of the underestimated ice thickness in the THIZ dataset. In this area, the THIZ dataset revealed zero ice thickness  
595 because of an overestimation of the bedrock elevation (Figure 3).

596

597



598

599

600 **Figure 9.** Maps of the modelled ice flux divergence for the different years under consideration. Contours are added for every  
601  $0.5$  m i.e.  $\text{yr}^{-1}$ . The background image is a Sentinel-2 true colour composite satellite image from 13 September 2020.

602

603

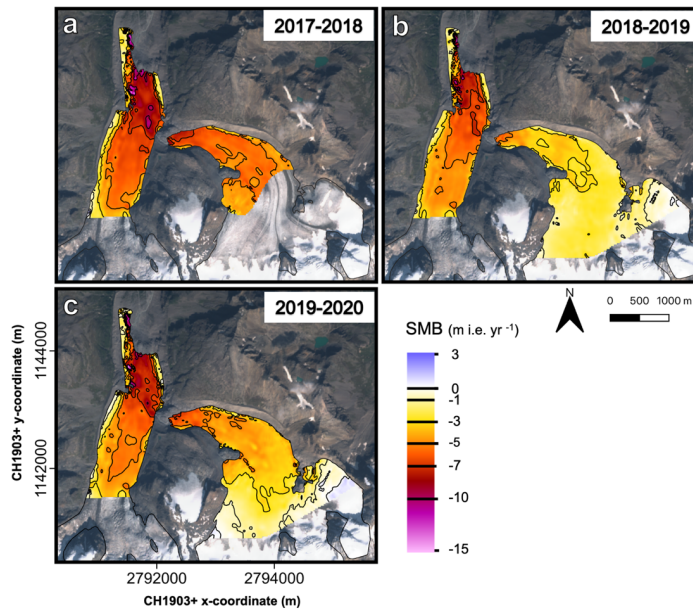
604 **4.4 SMB from UAV**

605

606 The final step of the method is to add the surface elevation changes (see Figure 6) and the computed ice flux  
607 divergence (Figure 9) to obtain the SMB (see Eq. 1). The final product, the modelled SMB for the three balance  
608 years, is shown in Figure 10. The three years in consideration clearly show a rather similar pattern. Areas with a  
609 less negative SMB are located at the same locations (e.g. western margin of Vadret da Morteratsch). Areas with  
610 the most negative SMB are also at the same location (e.g. glacier fronts). The ice flux divergence is prominently  
611 not able to compensate for the very negative SMB so that there is net mass loss everywhere and the altitude changes  
612 are less than zero. The most negative SMB (up to  $-13 \text{ m i.e. yr}^{-1}$ ) is found at the front of Vadret da Morteratsch in  
613 2017-2018 which is in accordance with the SMB measurements. This concerns the lowest area which is also quasi-  
614 stagnant with a very limited supply of ice from upstream (see Figure 9). The presence of certain irregular patches  
615 with a smaller or larger SMB is caused by artefacts in the flow correction method (see section 3.2 and Figure 6d).  
616 This is because the flow correction method cannot trace all displacements exactly (rocks fall over, crevasses  
617 deform, supraglacial melt streams are positioned on different locations etc.), and because the velocity field is not  
618 fully accurate, and the calculation of the longitudinal slope also affects the result.

619

620



621

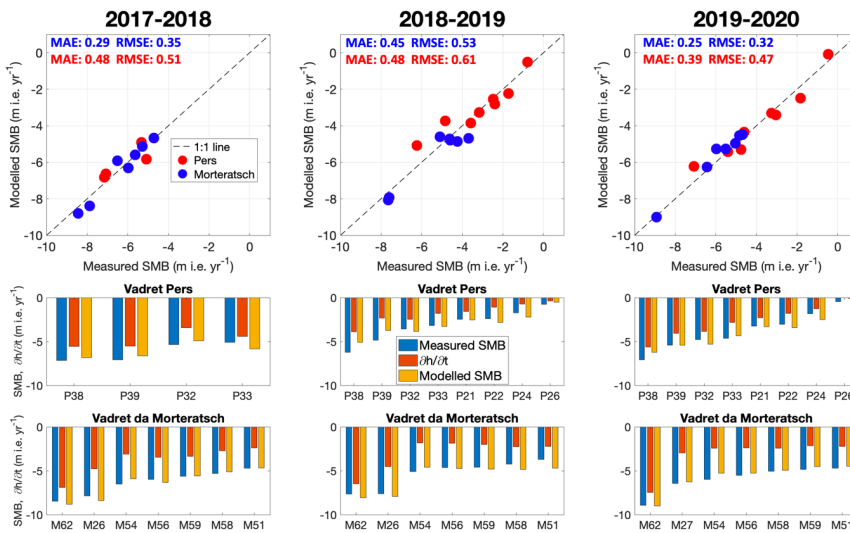
622 **Figure 10.** Maps of the modelled SMB fields. Contours are added for specific values (indicated on the colorbar). The  
623 background image is a Sentinel-2 true colour composite satellite image from 13 September 2020.

624

625

626 The associated point-by-point comparison between modelled and measured SMB confirms the good match with  
 627 deviations generally smaller than 0.5 m i.e. yr<sup>-1</sup> (Figure 11). The largest differences are found at the front of Vadret  
 628 Pers (Figure 11). Near the glacier front, the ice flux divergence is likely underestimated as a result of overestimated  
 629 ice thickness in this area of the THIZ dataset. The latter decreases the ice thickness gradient in this area  
 630 substantially.

632 In 2019, stake M26 (see Figure 2) was replaced by M27 (and installed at a higher location) because it was located  
 633 in the middle of a field of transverse crevasses during the survey in 2019. It is noticeable that this location was  
 634 characterised by a more negative SMB compared to the surrounding areas in both 2017-2018 and 2018-2019 (see  
 635 Figure 10 and Figure ) which is probably caused by a more exposed position on an ice serac.



638  
 639  
 640 **Figure 11.** Point-by-point comparison of modelled and measured SMB. In the lower panels, the difference between the  
 641 modelled SMB (yellow bar) and the local elevation change (red bar) results from the modelled ice flux divergence. The labels  
 642 refer to the stake names as used in the fieldwork programme. The MAE and RMSE of the modelled SMB are added in the upper  
 643 panels (Values are in m i.e yr<sup>-1</sup>).

646 For the optimal SMB fields, a minimum MAE of 0.25 m i.e. yr<sup>-1</sup> is obtained for Vadret da Morteratsch in 2019-  
 647 2020 (Figure ). The MAE and RMSE are somewhat larger for Vadret Pers with a maximum of 0.61 m i.e. yr<sup>-1</sup> in  
 648 2018-2019 which is mainly caused by the larger deviation for the lowest two stakes (Figure ).

heeft opmaak toegepast: Lettertype: 10 pt, Niet Vet, Niet  
 Cursief, Engels (Groot-Britannië), Afspatiëren op 16 pt

heeft verwijderd: Figure 2

heeft verwijderd: Figure 10

heeft verwijderd: Figure

heeft opmaak toegepast: Lettertype: 10 pt, Niet Cursief,  
 Engels (Groot-Britannië), Afspatiëren op 16 pt

heeft opmaak toegepast: Lettertype: 10 pt, Niet Cursief,  
 Engels (Groot-Britannië), Afspatiëren op 16 pt

heeft verwijderd: Figure

heeft opmaak toegepast: Lettertype: 10 pt, Niet Cursief,  
 Engels (Groot-Britannië), Afspatiëren op 16 pt

heeft opmaak toegepast: Lettertype: 10 pt, Niet Cursief,  
 Engels (Groot-Britannië), Afspatiëren op 16 pt

heeft verwijderd: Figure

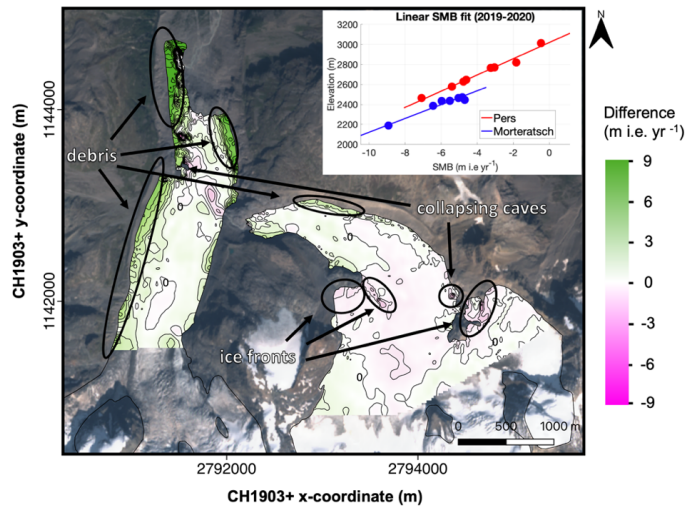
656 **4.5 Lateral variations in the SMB pattern**

657

658 Using the continuity method based on close-range (UAV) remote sensing data clearly reveals a much more detailed  
 659 picture of SMB than is possible from a stake network on a limited number of locations. This is evident in the  
 660 lateral heterogeneity of SMB, which is often overlooked when considering elevation as the prime variable to plan  
 661 the stake locations. In Figure 12 the difference is shown between the UAV-derived SMB field and a SMB field  
 662 only determined by elevation as derived from a linear fit of the stake measurements with altitude (see the inset of  
 663 Figure 12). In general, the largest differences occur close to the margin of the glaciers, and around their front. The  
 664 differences at the glacier margin of Vadret da Morteratsch are mainly related to a thick debris cover, which when  
 665 sufficient in thickness, has an insulating effect that reduces the glacier melt (e.g. Rounce et al., 2018; Verhaegen  
 666 et al., 2020). For example, for the heavily-debris covered area where Vadret da Morteratsch protrudes towards the  
 667 north, the SMB is -1.5 m i.e. yr<sup>-1</sup> below the debris and up to -12 m i.e. yr<sup>-1</sup> for the ice next to the debris. A thin  
 668 layer of debris, and the terminal ice cliff (Immerzeel et al., 2014), further reinforces the melt here, explaining this  
 669 very high ablation rate (Rossini et al., 2018). The melt ratio is therefore equal to 0.125, which means that there is  
 670 87.5% less melt under the debris at this location. This corresponds to a debris thickness of more than 50 cm when  
 671 a typical average value of the characteristic debris thickness is used (Anderson and Anderson, 2016; Rounce et al.,  
 672 2018). Such thicknesses are very likely in this area. During the fieldwork campaigns, boulder supply from the  
 673 moraines was observed on several occasions, which was also documented in the Himalaya by Van Woerkom et  
 674 al. (2019).

675

676



677

678 **Figure 12.** The inset shows a linear SMB fit based on stake measurements. The main figure shows the difference between the  
 679 UAV-derived SMB and the linearly derived SMB. The background image is a Sentinel-2 true colour composite satellite image  
 680 from 13 September 2020. Contour lines are added for every metre. Labels are added for the contour of value 0 m i.e. yr<sup>-1</sup>.

681

682

683 Another major feature is the presence of patches with a clearly more negative SMB when relying on the UAV-  
684 derived field. These differences relate to stationary areas at local ice fronts or collapsing ice caves. While  
685 the first are real SMB variations (caused by more irradiation and/or less snow), the latter ones are not caused by  
686 the SMB. These collapsing ice caves clearly appear to occur near stagnant ice and at the bottom of the glacier  
687 where melt water forms a cave below the ice (Figure 12). These caves collapse when the overlying ice becomes  
688 too thin due to melting at the surface. For the other areas, the difference between the SMB fields is generally  
689 smaller, between  $-0.5$  and  $0.5$  m i.e  $\text{yr}^{-1}$ . This is in the same order as the MAE and the RMSE and is slightly larger  
690 than the expected accuracy of the SMB measurements. The mean of the differences corresponds to  $0.56$  m i.e.  $\text{yr}^{-1}$ , which is specifically caused by the western side of the Morteratsch glacier with a thick layer of debris (see Figure  
691 2 and Figure 12). Using the simple linear fit to derive the SMB pattern would overestimate the ablation in the  
692 surveyed area with  $2.4 * 10^6 \text{ m}^3$ .  
693

694

695

## 696 5 Uncertainty analysis of the selected data, parameters and filters

697

698 The surface elevation changes and the ice flux divergence contribute separately to the surface mass balance,  
699 implying that errors and uncertainties in both terms do not influence each other but directly affect the determined  
700 SMB (Eq. 4). It is therefore crucial to determine to which extent the uncertainty of both affects the results of the  
701 applied method. In addition, we evaluate the results of the different filter procedures of the ice flux divergence.

702

### 703 5.1 Dependence on the data and F-value used

704

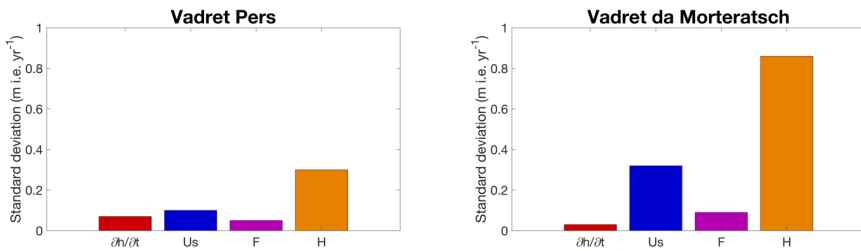
705 To study the dependence of the applied method to the uncertainty attributable to the used data and F-value, we  
706 create 100 perturbed fields of the surface elevation changes, the surface velocity, the F-value and the ice thickness.  
707 After that, we do the calculations, using the perturbed data for one dataset and the original data for the other ones.  
708 Next, the MAE of modelled versus measured SMB is calculated 100 times and for all years and the standard  
709 deviation of this MAE is determined. For the analysis, the different input fields are perturbed using random patches  
710 with a diameter (uniformly distributed) between 50 m (local errors at grid level) and 500 m with perturbation  
711 values normally distributed with a standard deviation of half the error estimate.

712 The uncertainty in the surface elevation changes is assumed to be correlated in space, i.e. depending on a pattern  
713 across the glacier (e.g. Fisher et al., 2015). Therefore, the  $\partial h/\partial t$  fields are perturbed with perturbations of maximum  
714 0.5 m (plausible maximum value for the multiannual  $\partial h/\partial t$  from UAV data) (see Table 2). Regarding surface  
715 velocity, we use error estimates of 10% of the observed velocity, similar to the expected accuracy (see section  
716 4.2). Besides velocity itself, the assumption of a constant F-value is rather unrealistic (Zekollari et al., 2013). Ice  
717 flow over basal irregularities causes variations in F. Previous research showed for example F to be larger over  
718 basal highs and smaller over basal lows and glacier areas with more basal sliding might as well be characterized  
719 by a larger F-value (Reeh et al., 2003). Therefore, we apply perturbations using an F-value between 0.85 and 0.95.

heeft verwijderd: value for UAV data

721 Concerning ice thickness, we apply perturbations with an error estimate of 30%, which is mentioned by Zekollari  
722 et al. (2013) as an estimate of the accuracy.

723  
724



725  
726

727 **Figure 13.** Standard deviation of the MAE for the perturbed versions of the surface elevation changes, the surface velocity  
728 ( $u_s$ ), the F-value and the ice thickness (H).

729  
730

731 The effect of perturbation of  $\partial h/\partial t$  on the determined SMB is small with a standard deviation of less than 0.1 m  
732 i.e.  $\text{yr}^{-1}$  for both glaciers (Figure 13). As a result, the results of the applied method are not very dependent on  
733 (small) perturbations in  $\partial h/\partial t$ . Changes in the F-value and surface velocity also appear to have minor sensitivity,  
734 especially concerning Vadret Pers. Regarding Vadret da Morteratsch, the surface velocity has a SD of 0.3 m i.e.  
735  $\text{yr}^{-1}$ , which is not negligible (Figure 13). The ice thickness distribution, however, is for both glaciers undoubtedly  
736 most crucial for the determination of the SMB, and even more so for Vadret da Morteratsch.

737

738 We therefore conducted some additional tests with both (THIZ and THIL) individual ice thickness datasets and  
739 for different combinations. For Pers glacier, the Langhammer dataset proved to be slightly better (MAE of 0.49  
740 versus 0.60 m i.e.  $\text{yr}^{-1}$ ), while for Morteratsch, the Zekollari dataset performed better (MAE of 0.74 versus 0.90 m  
741 i.e.  $\text{yr}^{-1}$ ). But in general, all combinations tested gave poorer results, which encouraged us to use the average ice  
742 thickness in this study. Further, it should be mentioned that the above analysis is valid for the glacier wide mean  
743 SMB deviations. For local point measurements, the uncertainty related to the used data, or the F-parameter, might  
744 be larger.

745  
746

## 747 5.2 Evaluation of procedures to filter the ice flux divergence

748

749 As the ice flow at a given location is determined by the surrounding glacier geometry (i.e. not only by its local  
750 geometry) and to avoid non-physical oscillations in the flux divergence field (as a result of fine grid spacing), it  
751 appears to be necessary to consider various spatial scales over which the ice flux divergence needed to be  
752 determined and different filtering procedures (see section 3.5). The results of each possible combination are shown  
753 in Figure 14.

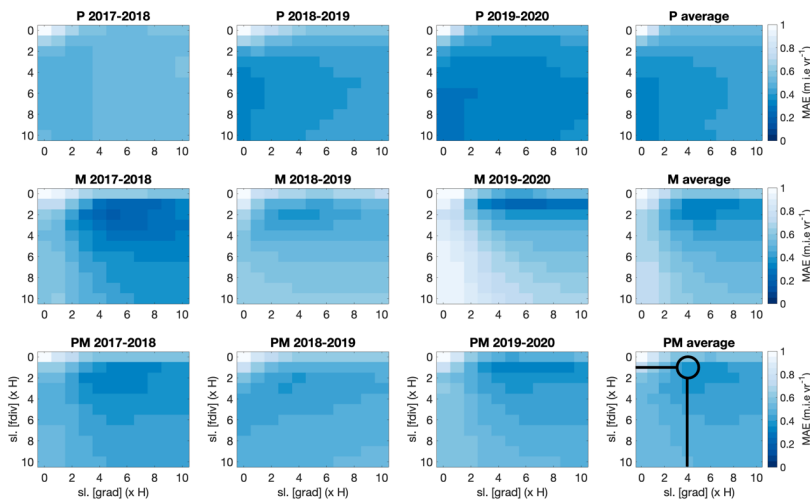
754

heeft verwijderd: , while for Morteratsch, the Zekollari dataset performed better

757 By only applying the exponential decay filter to the ice flux divergence field (moving down in the matrix), we find  
 758 minimum MAE and RMSE values when the scaling length is equal to five times H (MAE for Morteratsch-Pers is  
 759 0.51 m i.e.  $\text{yr}^{-1}$ ). Such a large scaling length indicates that the ice flux divergence field must be smoothed  
 760 significantly and therefore becomes entirely smeared with limited variation in the ablation area. One of the reasons  
 761 for this high value are large ice thickness and velocity gradients resulting from solving ice flow processes on a  
 762 high-resolution numerical grid. To compensate for the effects of large gradients, the second option is to consider  
 763 the gradients over larger spatial scales. We do this by applying the exponential filter to the ice thickness and  
 764 velocity gradients and calculate the ice flux divergence using these smoothed gradients (moving to the right in the  
 765 matrix). A minimum MAE of 0.54 m i.e.  $\text{yr}^{-1}$  is reached as soon as the velocity and ice thickness gradients are  
 766 considered over six times H. The solution to compensate for the negative effects of a very large scaling length for  
 767 both previous filters and the biases related to both is to filter twice, as was elucidated in section 3.4 and shown in  
 768 section 4.3. As soon as the ice thickness and velocity gradients and the ice flux divergence are smoothed, the MAE  
 769 becomes significantly smaller (Figure 14). The MAE is now much below 1 m i.e.  $\text{yr}^{-1}$ .

770

771



772

773

774 **Figure 14.** Mean absolute error between measured and modelled SMB for various scaling lengths. The scaling length depends  
 775 on the local ice thickness ( $x H$ ). Smoothing the ice thickness and velocity gradients (*grad*) or smoothing the ice flux divergence  
 776 (*fdiv*) is represented by the horizontal axis and vertical axis, respectively. *M* represents Vadret da Morteratsch, *P* represents  
 777 Vadret Pers and *PM* represents the entire glacier complex. The plots entitled with average concern the average over all balance  
 778 years. The selected combination with which the ice flux divergence is calculated as shown in Figure 9 is encircled with black.

779

780

781 Another observation standing out is that concerning Vadret Pers, the MAE mostly decreases when the ice flux  
 782 divergence is smoothed while for Vadret da Morteratsch, smoothing the gradients has a larger impact (See Figure  
 783 14). Our explanation for these peculiar differences is that the gradients (both in terms of ice thickness and surface

784 velocity) for Vadret Pers are already significantly smaller compared to those of Vadret da Morteratsch. The latter  
785 glacier has both a higher velocity and a larger ice thickness. Consequently, smoothing of the gradients for Vadret  
786 da Morteratsch is more decisive, whereas for Vadret Pers it is the other way around.

787

788 Other filters such as a mean filter or a Gaussian filter were explored, but all gave (slightly) less accurate results.  
789 However, our tests with a Gaussian filter showed only slightly larger errors for similar spatial scales. A Gaussian  
790 filter could therefore be a possible alternative to the exponential filter. Furthermore, the stakes used for validation  
791 were not entirely homogeneously distributed throughout the study area. The accuracy analysis may therefore have  
792 been biased towards these locations, which may also have influenced the choice of the optimal filter (length).

793

## 794 6 Transferability of the method

795

796 Our study shows that with the continuity equation method, the SMB at the position of the stakes can be accurately  
797 estimated. It therefore seems to be a promising method for supplementing SMB stake measurements on glaciers.  
798 To convert the results presented here to the conventional unit of mass balance, assumptions must be made for  
799 density. In the ablation area, to which our study area was limited, the SMB could have been converted directly to  
800 metres of water equivalent using an average ice density such as  $900 \text{ kg/m}^3$ . However, when the presented method  
801 would be applied to for example the accumulation area, specific attention is required for each quantity of the  
802 continuity equation (Miles et al., 2021).

803

804 The applicability of the method to other, less well studied glaciers, depends on how closely the elevation changes,  
805 the surface velocities and the ice thickness can be estimated for these ice bodies. In recent years, a new series of  
806 methods have arisen from which surface elevation changes and surface velocities can be rather accurately derived  
807 over glaciers (Brun et al., 2017; Paul et al., 2017; Braun et al., 2019; Nagy et al., 2019; Dussaillant et al., 2019;  
808 Sommer et al., 2020). This seems encouraging to investigate the applicability using satellite data with a resolution  
809 which should preferably be smaller than 10 m for accurate velocity determination. However, our analysis also  
810 showed that especially the ice thickness should be known well. So far, the ice thickness has only been measured  
811 for less than 0.5% of all glaciers on Earth. As shown in a recent study on four Central Asian glaciers, large-scale  
812 thickness estimates may capture the general pattern of the ice thickness distribution and total volume well, yet  
813 exhibit significant deviations at the local scale (Van Tricht et al., 2021). To apply the proposed method on glaciers  
814 where the ice thickness has not been measured, estimated ice thickness such as the consensus estimate might seem  
815 a viable option (Farinotti et al., 2019). To evaluate the use of the consensus estimate, we also computed the SMB  
816 using our method and the consensus estimate, for our optimal settings. Concerning Vadret Pers, the MAE and SEE  
817 were quite similar (0.52 and 0.62 m i.e.  $\text{yr}^{-1}$  respectively) while for Vadret da Morteratsch, the MAE and SEE were  
818 considerably higher (1.08 and 1.22 m i.e.  $\text{yr}^{-1}$  respectively). The latter is likely the result of the ice thickness being  
819 significantly too small in the consensus estimate (223 meters while we measured 297 m in 2020). This leaves the  
820 question open whether the method can be applied to glaciers where the ice thickness is not measured or known  
821 well. Further testing could be performed on other glaciers for which multiannual high-resolution topographic data  
822 already exist from repeated UAV surveys (e.g. Immerzeel et al., 2014; Kraaijenbrink et al., 2016; Wigmore et al.,  
823 2017; Benoit et al., 2019; Groos et al., 2019; Yang et al., 2020; Vincent et al., 2021).

heeft verwijderd: Concerning Vadret Pers, the MAE and SEE were quite similar while for Vadret da Morteratsch, the MAE and SEE were considerably higher.

827  
828  
829  
830  
831  
832  
833  
834  
835  
836  
837  
838  
839  
840  
841  
842  
843  
844  
845  
846  
847  
848  
849  
850  
851  
852  
853  
854  
855  
856  
857  
858  
859  
860  
861  
862  
863  
864  
865  
866  
867

## 7 Conclusions

In this study, a method was presented to estimate the surface mass balance pattern from UAV observations, a known ice thickness field, and the principles of mass continuity. Annual surface elevation changes and surface velocities were quantified from UAV and were shown to have centimetre accuracy. The method was applied to the entire ablation zone of Vadret da Morteratsch and Vadret Pers (Switzerland) for three individual balance years between 2017 and 2020. For the well-studied Morteratsch-Pers glacier complex, we were able to closely reproduce SMB surveyed at about 16 stake locations. A major advantage of using close-range (UAV) remote sensing data is that a significantly more detailed SMB pattern can be obtained over the entire ablation area at a high spatial resolution, which is not feasible with a (small) number of stakes. This avoids the need for interpolation and extrapolations from a limited number of stakes, which can introduce several significant errors when the heterogeneity of the glacier surface cannot be captured well from the installed stake positions.

The analysis did not demonstrate a simple consensus on how to consider the ice flux divergence for optimal results on both glaciers. It proved to be necessary to consider large spatial scales concerning the ice flux divergence to apply the continuity-equation method and closely reproduce the SMB at the position of ablation stakes. By using an exponential decay filter to the ice thickness and velocity gradients and the ensuing ice flux divergence over several times the local ice thickness (at least  $2x$ ), the mean absolute error between modelled and measured SMB decreased to 0.25-0.61 m i.e.  $\text{yr}^{-1}$  for the three balance years. Considering the uncertainty of the data and the stake measurements themselves, this is quite accurate. Our study therefore offers a transferable method that can be used, as long as the ice thickness is sufficiently well known, to estimate the SMB pattern from UAV data. With the increasing resolution of satellite data, we are convinced that the method presented here for UAV data will eventually be able to be used for satellite data as well, allowing it to be easily transferred to other glaciers and regions.

## Code and data availability

The model code written in MATLAB, which was used as the basis for this research, can be found and downloaded from <https://github.com/LanderVT/SMB-from-UAV>. The other input datasets and the UAV created DSMs will be provided on request by Lander Van Tricht.

## Author contribution

868 LVT developed the method, performed the experiments and wrote the manuscript. PH provided guidance in  
869 implementing the research and interpreting the results and assisted during the entire process. JVB and AV  
870 contributed to the fieldwork, collaborated in developing the method and improved the manuscript throughout the  
871 entire process. KVO assisted during the fieldwork and introduced LVT in using UAVs for research purposes. HZ  
872 participated in the fieldwork for many years and contributed throughout the entire process to developing the  
873 method and optimising and refining the research.

874

875

#### 876 **Competing interests.**

877

878 The authors declare that they have no conflict of interest.

879

880

#### 881 **Acknowledgements**

882

883 The authors would like to thank Chloe Marie Paice, Felix Vanderleenen, He Zhang, Robbe Neyns, Steven De  
884 Hertog, Veronica Tollenaar and Yoni Verhaegen, who assisted during the fieldwork to perform stake  
885 measurements and distribute and collect GCPs.

886

887

#### 888 **Financial Support**

889

890 Lander Van Tricht holds a PhD fellowship of the Research Foundation-Flanders (FWO-Vlaanderen) and is  
891 affiliated with the Vrije Universiteit Brussel (VUB). Harry Zekollari contributed to the fieldwork as a PhD fellow  
892 of the Research Foundation-Flanders (FWO-Vlaanderen) and at a later stage as a Marie Skłodowska-Curie fellow  
893 at the TU Delft (grant 799904). K Van Oost is an FNRS Research Director.

894

895

#### 896 **Review statement.**

897

898 This paper was edited by Etienne Berthier and reviewed by Evan Miles, Alexander Raphael Groos, and one  
899 anonymous reviewer.

900

901

902 **8 References**

903

904 Anderson, L.S. and Anderson, R.S.: Modeling debris-covered glaciers: response to steady  
905 debris deposition, *The Cryosphere*, 10, 1105–1124, <https://doi.org/10.5194/tc-10-1105-2016>, 2016

906

907 Benoit, L., Gourdon, A., Vallat, R., Irrazaval, I., Gravey, M., Lehmann, B., Prasicek, G., Gräff, D., Herman,  
908 F. and Mariethoz, G.: A high-resolution image time series of the Gorner Glacier – Swiss Alps – derived  
909 from repeated unmanned aerial vehicle surveys, *Earth Syst. Sci. Data*, 11, 579–588,  
910 <https://doi.org/10.5194/essd-11-579-2019>, 2019

911

912 Berthier, E. and Vincent, C.: Relative contribution of surface mass-balance and ice-flux changes to the  
913 accelerated thinning of Mer de Glace, French Alps, over 1979-2008, *Journal of Glaciology*, 58(209),  
914 501-512, <https://doi.org/10.3189/2012JoG11J083>, 2012

915

916 Bisset, R.R., Dehecq, A., Goldberg, D.N., Huss, M., Bingham, R.G. and Gourmelen, N.: Reversed Surface-  
917 Mass-Balance Gradients on Himalayan Debris-Covered Glaciers Inferred from Remote Sensing, 12,  
918 <https://doi.org/10.3390/rs12101563>, 2020.

919

920 Braithwaite, R.J.: Glacier mass balance: the first 50 years of international monitoring, *Progress in Physical*  
921 *Geography*, 26, 76–95, <https://doi.org/10.1191/0309133302pp326ra>, 2002

922

923 Braun, M.H., Malz, P., Sommer, C., Fariás-Barahona, D., Sauter, T., Casassa, G., Soruco, A., Skvarca, P. and  
924 Seehaus, T.C.: Constraining glacier elevation and mass changes in South America, *Nature Climate*  
925 *Change*, 9(2), 130–136, <https://doi.org/10.1038/s41558-018-0375-7>, 2019

926

927 Brun, F., Berthier, E., Wagnon, P., Kääb, A. and Treichler, D.: A spatially resolved estimate of High Mountain  
928 Asia glacier mass balances from 2000 to 2016, *Nature Geoscience*, 10, 668–673,  
929 <https://doi.org/10.1038/ngeo2999>, 2017

930

931 Brun, F., Wagnon, P., Berthier, E., Shea, J. M., Immerzeel, W. W., Kraaijenbrink, P. D. A., Vincent, C.,  
932 Reverchon, C., Shrestha, D. and Arnaud, Y.: Ice cliff contribution to the tongue-wide ablation of  
933 Changri Nup Glacier, Nepal, central Himalaya, *The Cryosphere*, 12, 3439–3457,  
934 <https://doi.org/10.5194/tc-12-3439-2018>, 2018

935

936 Davaze, L., Rabatel, A., Dufour, A., Hugonnet, R. and Arnaud, Y.: Region-Wide Annual Glacier Surface  
937 Mass Balance for the European Alps From 2000 to 2016, *Frontiers in Earth Science*, 8, 0–14,  
938 <https://doi.org/10.3389/feart.2020.00149>, 2020

939

940

941

942 Dussailant, I., Berthier, E., Brun, F., Masiokas, M., Hugonnet, R., Favier, V., Rabatel, A., Pitte, P. and Ruiz, L.:  
943 Two decades of glacier mass loss along the Andes, *Nature Geoscience*, 12, 802–808,  
944 <https://doi.org/10.1038/s41561-019-0432-5>, 2019  
945  
946 Farinotti, D., Huss, M., Fürst, J.J., Landmann, J., Machguth, H., Maussion, F. and Pandit, A.: A consensus  
947 estimate for the ice thickness distribution of all glaciers on Earth, *Nat. Geosci.*, 1,  
948 <https://doi.org/10.1038/s41561-019-0300-3>, 2019  
949  
950 Fischer, M., Huss, M. and Hoelzle, M.: Surface elevation and mass changes of all Swiss glaciers 1980–  
951 2010, *The Cryosphere*, 9, 525–540, <http://doi.org/10.5194/tc-9-525-2015>, 2015  
952  
953 Gindraux, S., Boesch, R. and Farinotti, D.: Accuracy Assessment of Digital Surface Models from  
954 Unmanned Aerial Vehicles’ Imagery on Glaciers, *Remote Sensing*, 9(2),  
955 186, <https://doi.org/10.3390/rs9020186>, 2017  
956  
957 Goldstein, E.B., Oliver, A.R., deVries, E., Moore, L.J. and Jass, T.: Ground control point requirements for  
958 structure-from-motion derived topography in low-slope coastal environments, *PeerJPrePrints*  
959 3:e1444v1, <https://doi.org/10.7287/peerj.preprints.1444v1>, 2015  
960  
961 Groos, A.R., Bertschinger, T.J., Kummer, C.M., Erlwein, S., Munz, L. and Philipp, A.: The Potential of Low-  
962 Cost UAVs and Open-Source Photogrammetry Software for High-Resolution Monitoring of Alpine  
963 Glaciers: A Case Study from the Kanderfirn (Swiss Alps), *Geosciences* 9, 1–21,  
964 <https://doi.org/10.3390/geosciences9080356>, 2019  
965  
966 Gudmundsson, G.H. and Bauder, A.: Towards an Indirect Determination of the Mass-balance Distribution of  
967 Glaciers using the Kinematic Boundary Condition, *Geografiska Annaler*, 81(4), 575–583,  
968 <https://doi.org/10.1111/1468-0459.00085>, 1999  
969  
970 Heid, T. and Kääb, A.: Evaluation of existing image matching methods for deriving glacier surface  
971 displacements globally from optical satellite imagery, *Remote Sensing of Environment*, 118, 339–355,  
972 <https://doi.org/10.1016/j.rse.2011.11.024>, 2012  
973  
974 Hubbard, A., Willis, I., Sharp, M., Mair, D., Nienow, P., Hubbard, B. and Blatter, H.: Glacier mass-balance  
975 determination by remote sensing and high-resolution modelling, *Journal of Glaciology*, 46(154), 491–  
976 498, <https://doi.org/10.3189/172756500781833016>, 2000  
977  
978 Huss, M., Dhulst, L. and Bauder, A.: New long-term mass-balance series for the Swiss Alps, *Journal of*  
979 *Glaciology*, 61(227), 551–562, <https://doi.org/10.3189/2015JoG15J015>, 2015  
980  
981

982  
983 Hutter, R.K. and Morland, L.W.: Euromech colloquium 172: Mechanics of glaciers, Interlaken, 19–23  
984 September, 1983, *Cold Regions Science and Technology*, 9(1), 77-86, [https://doi.org/10.1016/0165-](https://doi.org/10.1016/0165-232X(84)90049-1)  
985 [232X\(84\)90049-1](https://doi.org/10.1016/0165-232X(84)90049-1), 1984  
986  
987 Immerzeel, W.W., Kraaijenbrink, P.D.A., Shea, J.M., Shrestha, A.B., Pellicciotti, F., Bierkens, M.F.P. and de  
988 Jong, S.M.: High-resolution monitoring of Himalayan glacier dynamics using unmanned aerial vehicles,  
989 *Remote Sensing of Environment*, 150, 93–103, <https://doi.org/10.1016/j.rse.2014.04.025>, 2014  
990  
991 Kääb, A. and Funk, M.: Modelling mass balance using photogrammetric and geophysical data: a pilot  
992 Study at Griesgletscher, Swiss Alps, *Journal of Glaciology*, 45(151), 575–583,  
993 <https://doi.org/10.3189/S0022143000001453>, 1999  
994  
995 Kamb, B. and Echelmeyer, K.A.: Stress-gradient Coupling in Glacier Flow: IV. Effects of the “ T ”  
996 Term, *Journal of Glaciology*, 32(112), 342–349, <https://doi.org/10.3189/S0022143000012016>, 1986  
997  
998 Kaser, G., Fountain, A. and Jansson, P.: A manual for monitoring the mass balance of mountain glaciers,  
999 *International Hydrological Programme (IHP-VI. Technical Documents in Hydrology 59)*, UNESCO,  
1000 Paris, 2003.  
1001  
1002 Kienholz, C., Pierce, J., Hood, E., Amundson, J.M., Wolken, G.J., Jacobs, A., Hart, S., Wikstrom, Jones K.,  
1003 Abdel-Fattah, D., Johnson, C. and Conaway, J.S.: Deglaciation of a Marginal Basin and  
1004 Implications for Outburst Floods, Mendenhall Glacier, Alaska. *Frontiers in Earth Science*, 8, 1–21  
1005 <https://doi.org/10.3389/feart.2020.00137>, 2020  
1006  
1007 Kraaijenbrink, P., Meijer, S.W., Shea, J.M., Pellicciotti, F., De Jong, S.M. and Immerzeel, W.W.: Seasonal  
1008 surface velocities of a Himalayan glacier derived by automated correlation of unmanned aerial vehicle  
1009 imagery, *Annals of Glaciology* 57, 103–113, <https://doi.org/10.3189/2016AoG71A072>, 2016  
1010  
1011 Langhammer, L., Grab, M., Bauder, A. and Maurer, H.: Glacier thickness estimations of alpine glaciers  
1012 using data and modeling constraints, *The Cryosphere*, 13(8), 2189–2202, [https://doi.org/10.5194/tc-13-](https://doi.org/10.5194/tc-13-2189-2019)  
1013 [2189-2019](https://doi.org/10.5194/tc-13-2189-2019), 2019  
1014  
1015 Le Brocq, A.M., Payne, A.J. and Siegert, M.J.: West Antarctic balance calculations: Impact of flux-routing  
1016 algorithm, smoothing algorithm and topography. *Computers and Geosciences*, 32(10), 1780–1795,  
1017 <https://doi.org/10.1016/j.cageo.2006.05.003>, 2006  
1018  
1019  
1020  
1021

1022 Long, N., Millescamps, B., Pouget, F., Dumon, A., Lachaussée, N. and Bertin, X.: Accuracy assessment of  
1023 coastal topography derived from UAV images, *The International Archives of the Photogrammetry,*  
1024 *Remote Sensing and Spatial Information Sciences*, XLI-B1, 1127–1134, [https://doi.org/10.5194/isprs-](https://doi.org/10.5194/isprs-archives-XLI-B1-1127-2016)  
1025 [archives-XLI-B1-1127-2016](https://doi.org/10.5194/isprs-archives-XLI-B1-1127-2016), 2016  
1026  
1027 Marzeion, B., Hock, R., Anderson, B., Bliss, A., Champollion, N., Fujita, K., Huss, M., Immerzeel, W.W.,  
1028 Kraaijenbrink, P., Malles, J., Maussion, F., Radić, V., Rounce, D.R., Sakai, A., Shannon, S., Wal, R.  
1029 and Zekollari, H.: Partitioning the Uncertainty of Ensemble Projections of Global Glacier Mass Change,  
1030 *Earth's Future*, 8(7), 1–25, <https://doi.org/10.1029/2019EF001470>, 2020  
1031  
1032 Messerli, A. and Grinsted, A.: Image georectification and feature tracking toolbox: ImGRAFT, *Geoscientific*  
1033 *Instrumentation Methods and Data Systems*, 4, 23–34, <https://doi.org/10.5194/gi-4-23-2015>, 2015  
1034  
1035 Miles, E., McCarthy, M., Dehecq, A., Kneib M., Fugger S. and Pellicciotti F.: Health and sustainability of  
1036 glaciers in High Mountain Asia, *Nat Commun* 12, 2868, <https://doi.org/10.1038/s41467-021-23073-4>,  
1037 2021  
1038  
1039 Millan, R., Mouginot, J., Rabatel, A., Jeong, S., Cusicanqui, D., Derkacheva, A. and Chekki, M.: Mapping  
1040 Surface Flow Velocity of Glaciers at Regional Scale Using a Multiple Sensors Approach, 11,  
1041 <https://doi.org/10.3390/rs11212498>, 2019  
1042  
1043 Nagy, T., Andreassen, L.M., Duller, R.A. and Gonzalez, P.J.: SenDiT: The Sentinel-2 Displacement Toolbox  
1044 with Application to Glacier Surface Velocities. *Remote Sensing*, 11(10), 1151,  
1045 <https://doi.org/10.3390/rs11101151>, 2019  
1046  
1047 Nemeč, J., Huybrechts, P., Rybak, O. and Oerlemans, J.: Reconstruction of the annual balance of  
1048 Vadret da Morteratsch, Switzerland, since 1865, *Annals of Glaciology*, 50(50), 126–134,  
1049 <https://doi.org/10.3189/172756409787769609>, 2009  
1050  
1051 Nuimura, T., Fujita, K., Fukui, K., Asahi, K., Aryal, R. and Ageta, Y.: Temporal Changes in Elevation of the  
1052 Debris-Covered Ablation Area of Khumbu Glacier in the Nepal Himalaya since 1978, *Arctic Antarctic*  
1053 *Alpine Research*, 43(2), 246–255, <https://doi.org/10.1657/1938-4246-43.2.246>, 2011  
1054  
1055 Paul, F., Bolch, T., Briggs, K., Kääb, A., McMillan, M., McNabb, R., Nagler, T., Nuth, C., Rastner, P., Strozzi,  
1056 T. and Wuite, J.: Error sources and guidelines for quality assessment of glacier area, elevation change,  
1057 and velocity products derived from satellite data in the Glaciers\_cci project. *Remote Sensing of*  
1058 *Environment*, 203, 256–275, <https://doi.org/10.1016/j.rse.2017.08.038>, 2017  
1059  
1060  
1061

1062 Reeh, N., Mohr, J.J., Krabill, W.B., Thomas, R., Oerter, H., Gundestrup, N. and Bøggild, C.E.: Glacier specific  
1063 ablation rate derived by remote sensing measurements. *Geophysical Research Letters*, 29(16), 10-1-10-  
1064 4, <https://doi.org/10.1029/2002GL015307>, 2002  
1065  
1066 Reeh, N., Mohr, J.J., Madsen, S.N., Oerter, H. and Gundestrup, N.S.: Three-dimensional surface velocities  
1067 of Storstrømmen glacier, Greenland, derived from radar interferometry and ice-sounding radar  
1068 measurements, *Journal of Glaciology*, 49(165), 201–209,  
1069 <https://doi.org/10.3189/172756503781830818>, 2003  
1070  
1071 Reznichenko, N., Davies, T., Shulmeister, J. and McSaveney, M.: Effects of debris on ice-surface melting  
1072 rates: an experimental study, *Journal of Glaciology*, 56(197), 384–394,  
1073 <https://doi.org/10.3189/002214310792447725>, 2010  
1074  
1075 Rossini, M., Di Mauro, B., Garzonio, R., Baccolo, G., Cavallini, G., Mattavelli, M., De Amicis, M. and  
1076 Colombo, R.: Rapid Melting Dynamics of an Alpine Glacier with Repeated UAV  
1077 Photogrammetry. *Geomorphology*, 304, 159–172, <https://doi.org/10.1016/j.geomorph.2017.12.039>,  
1078 2018  
1079  
1080 Rounce, D.R., King, O., McCarthy, M., Shean, D.E. and Salerno, F.: Quantifying Debris Thickness of Debris-  
1081 Covered Glaciers in the Everest Region of Nepal Through Inversion of a Subdebris Melt Model. *Journal*  
1082 *of Geophysical Research Earth Surface*, 123(5), 1094–1115, <https://doi.org/10.1029/2017JF004395>,  
1083 2018  
1084  
1085 Ruiz, L., Berthier, E., Masiokas, M., Pitte, P. and Villalba, R.: First surface velocity maps for glaciers of  
1086 Monte Tronador, North Patagonian Andes, derived from sequential Pléiades satellite images, *Journal of*  
1087 *Glaciology*, 61(229), 908–922, <https://doi.org/10.3189/2015JoG14J134>, 2015  
1088  
1089 Ryan, J.C., Hubbard, A.L., Box, J.E., Todd, J., Christoffersen, P., Carr, J.R., Holt, T.O. and Snooke N.: UAV  
1090 photogrammetry and structure from motion to assess calving dynamics at Store Glacier, a large outlet  
1091 draining the Greenland ice sheet, *The Cryosphere*, 9(1), 1–11, <https://doi.org/10.5194/tc-9-1-2015>, 2015  
1092  
1093 Seroussi, H., Morlighem, M., Rignot, E., Larour, E., Aubry, D., Ben Dhia, H. and Kristensen, S.S.: Ice flux  
1094 divergence anomalies on 79north Glacier, Greenland, *Geophysical Research Letters*, 38(9), L09501,  
1095 <https://doi.org/10.1029/2011GL047338>, 2011  
1096  
1097 Sommer, C., Malz, P., Seehaus, T.C., Lippl, S., Zemp, M. and Braun, M.H.: Rapid glacier retreat and  
1098 downwasting throughout the European Alps in the early 21st century, *Nature Communications*, 11(1),  
1099 3209, <https://doi.org/10.1038/s41467-020-16818-0>, 2020  
1100  
1101

1102 Tahar, K.N., Ahmad, A., Aziz, W.A., Akib, W.M., Mohd, W. and Mohd, N.W.: Assessment on Ground Control  
1103 Points in Unmanned Aerial System Image Processing for Slope Mapping Studies. *International Journal*  
1104 *of Scientific & Engineering Research*, 3(11), 1-10, 2012

1105

1106 Tonkin, T. and Midgley, N.: Ground-Control Networks for Image Based Surfac Reconstruction: An  
1107 Investigation of Optimum Survey Designs Using UAV Derived Imagery and Structure-from-Motion  
1108 Photogrammetry, *Remote Sensing*, 8(9), 786, <https://doi.org/10.3390/rs8090786>, 2016

1109

1110 Van Tricht, L., Huybrechts, P., Van Breedam, J., Fürst, J.J., Rybak, O., Satylkanov, R., Ermenbaiev, B., Popovnin,  
1111 V., Neyns, R., Paice, C.M. and Malz, P.: Measuring and inferring the ice thickness distribution of four  
1112 glaciers in the Tien Shan, Kyrgyzstan, *Journal of Glaciology*, 1–18, <https://doi.org/10.1017/jog.2020.104>,  
1113 2021

1114

1115 Van Woerkom, T., Steiner, J. F., Kraaijenbrink, P. D. A., Miles, E. S. and Immerzeel, W.W.: Sediment supply  
1116 from lateral moraines to a debris-covered glacier in the Himalaya. *Earth Surface Dynamics*, 7(2), 411–  
1117 427. <https://doi.org/10.5194/esurf-7-411-2019>, 2019

1118

1119 Verhaegen, Y., Huybrechts, P., Rybak, O. and Popovnin, V.V.: Modelling the evolution of Djankuat Glacier,  
1120 North Caucasus, from 1752 until 2100 CE, *The Cryosphere*, 14, 4039–4061, [https://doi.org/10.5194/tc-](https://doi.org/10.5194/tc-14-4039-2020)  
1121 [14-4039-2020](https://doi.org/10.5194/tc-14-4039-2020), 2020.

1122

1123 Vincent, C., Wagon, P., Shea, J.M., Immerzeel, W.W., Kraaijenbrink, P., Shrestha, D., Soruco, A., Arnaud,  
1124 Y., Brun, F., Berthier, E. and Sherpa, S.F.: Reduced melt on debris-covered glaciers: investigations  
1125 from Changri Nup Glacier, Nepal, *The Cryosphere*, 10, 1845–1858, [https://doi.org/10.5194/tc-10-1845-](https://doi.org/10.5194/tc-10-1845-2016)  
1126 [2016](https://doi.org/10.5194/tc-10-1845-2016), 2016.

1127

1128 Vincent, C., Cusicanqui, D., Jourdain, B., Laarman, O., Six, D., Gilbert, A., Walpersdorf, A., Rabatel, A., Piard,  
1129 L., Gimbert, F., Gagliardini, O., Peyaud, V., Arnaud, L., Thibert, E., Brun, F. and Nanni, U.: Geodetic  
1130 point surface mass balances: a new approach to determine point surface mass balances on glaciers from  
1131 remote sensing measurements, *The Cryosphere*, 15, 1259–1276, [https://doi.org/10.5194/tc-15-1259-](https://doi.org/10.5194/tc-15-1259-2021)  
1132 [2021](https://doi.org/10.5194/tc-15-1259-2021), 2021

1133

1134 Wagon, P., Brun, F., Khadka, A., Berthier, E., Shrestha, D., Vincent, C., Arnaud Y., Six D., Dehecq A.,  
1135 Ménégoz M. and Jomelli, V.: Reanalysing the 2007–19 glaciological mass-balance series of Mera  
1136 Glacier, Nepal, Central Himalaya, using geodetic mass balance, *Journal of Glaciology*, 67(261), 117-  
1137 125, <https://doi.org/10.1017/jog.2020.88>, 2021

1138

1139 Whitehead, K., Moorman, B.J. and Hugenholtz, C.H.: Brief Communication: Low-cost, on-demand aerial  
1140 photogrammetry for glaciological measurement, *The Cryosphere*, 7, 1879–1884,  
1141 <https://doi.org/10.5194/tc-7-1879-2013>, 2013.

1142  
1143 Wigmore, O. and Mark, B.: Monitoring tropical debris-covered glacier dynamics from high-resolution  
1144 unmanned aerial vehicle photogrammetry, Cordillera Blanca, Peru, *The Cryosphere*, 11, 2463–2480,  
1145 <https://doi.org/10.5194/tc-11-2463-2017>, 2017.  
1146  
1147 Wouters, B., Gardner, A.S. and Moholdt, G.: Global Glacier Mass Loss During the GRACE Satellite  
1148 Mission (2002–2016), *Frontiers in Earth Science*, 7, 1–11, <https://doi.org/10.3389/feart.2019.00096>,  
1149 2019  
1150  
1151 Yang, W., Zhao, C., Westoby, M., Yao, T., Wang, Y., Pellicciotti, F., Zhou, J., He, Z. and Miles, E.: Seasonal  
1152 Dynamics of a Temperate Tibetan Glacier Revealed by High-Resolution UAV Photogrammetry and In  
1153 Situ Measurements, *Remote Sensing*, 12(15), 2389, <https://doi.org/10.3390/rs12152389>, 2020  
1154  
1155 Zekollari, H., Huybrechts, P., Fürst, J.J., Rybak, O. and Eisen, O.: Calibration of a higher-order 3-D ice-  
1156 flow model of the Morteratsch glacier complex, Engadin, Switzerland, *Annals of Glaciology*, 54(63),  
1157 343–351, <https://doi.org/10.3189/2013AoG63A434>, 2013  
1158  
1159 Zekollari, H., Fürst, J.J. and Huybrechts, P.: Modelling the evolution of Vadret da Morteratsch,  
1160 Switzerland, since the Little Ice Age and into the future, *Journal of Glaciology*, 60(224), 1155–1168,  
1161 <https://doi.org/10.3189/2014JoG14J053>, 2014  
1162  
1163 Zekollari, H. and Huybrechts, P.: On the climate–geometry imbalance, response time and volume–area  
1164 scaling of an alpine glacier: insights from a 3-D flow model applied to Vadret da Morteratsch,  
1165 Switzerland, *Annals of Glaciology*, 56(70), 51–62, <https://doi.org/10.3189/2015AoG70A921>, 2015  
1166  
1167 Zekollari, H. and Huybrechts, P.: Statistical modelling of the surface mass-balance variability of the  
1168 Morteratsch glacier, Switzerland: strong control of early melting season meteorological conditions,  
1169 *Journal of Glaciology*, 64(244), 275–288, <https://doi.org/10.1017/jog.2018.18>, 2018  
1170  
1171 Zekollari, H., Huss, M. and Farinotti, D.: Modelling the future evolution of glaciers in the European Alps under  
1172 the EURO-CORDEX RCM ensemble, *The Cryosphere*, 13, 1125–1146, [https://doi.org/10.5194/tc-13-](https://doi.org/10.5194/tc-13-1125-2019)  
1173 [1125-2019](https://doi.org/10.5194/tc-13-1125-2019), 2019.  
1174  
1175 Zemp, M., Thibert, E., Huss, M., Stumm, D., Denby, C.R., Nuth, C., Nussbaumer, S.U., Moholdt, G., Mercer,  
1176 A., Mayer, C., Joerg, P.C., Jansson, P., Hynek, B., Fischer, A., Escher-Vetter, H., Elvehøy, H. and  
1177 Andreassen, L.M.: Uncertainties and re-analysis of glacier mass balance measurements Uncertainties  
1178 and re-analysis of glacier mass balance measurements, *The Cryosphere Discussions*, 7(2), 789–839,  
1179 <https://doi.org/10.5194/tcd-7-789-2013>, 2013  
1180  
1181

1182 Zemp, M., Huss, M., Thibert, E., Eckert, N., McNabb, R., Huber, J., Barandun, M., Machguth, H., Nussbaumer,  
1183 S.U., Gärtner-Roer, I., Thomson, L., Paul, F., Maussion, F., Kutuzov, S. and Cogley, J.G.: Global  
1184 glacier mass changes and their contributions to sea-level rise from 1961 to 2016, *Nature*, 568, 382–386,  
1185 <https://doi.org/10.1038/s41586-019-1071-0>, 2019  
1186  
1187 Zhang, H., Aldana-Jague, E., Clapuyt, F., Wilken, F., Vanacker, V. and Van Oost, K.: Evaluating the potential  
1188 of post-processing kinematic (PPK) georeferencing for UAV-based structure- from-motion (SfM)  
1189 photogrammetry and surface change detection, *Earth Surf. Dynam.*, 7, 807–827,  
1190 <https://doi.org/10.5194/esurf-7-807-2019>, 2019.  
1191  
1192  
1193